

# Nitric oxide feedback to ciliary photoreceptor cells gates a UV avoidance circuit

Kei Jokura<sup>1,\*</sup>, Nobuo Ueda<sup>2</sup>, Martin Gühmann<sup>3</sup>, Luis Alfonso Yañez-Guerra<sup>1</sup>, Piotr Słowiński<sup>1</sup>, Kyle C. A. Wedgwood<sup>1</sup> and Gáspár Jékely<sup>1,4,\*</sup>

<sup>1</sup>Living Systems Institute, University of Exeter, Stocker road, Exeter, EX4 4QD, United Kingdom <sup>2</sup>Okinawa Institute of Science and Technology, Okinawa, Japan, <sup>3</sup>School of Biological Sciences, University of Bristol, Bristol, United Kingdom, <sup>4</sup>Centre for Organismal Studies (COS), University of Heidelberg, 69120 Heidelberg, Germany

\*Correspondence : k.jokura @ exeter.ac.uk, gaspar.jekely @ cos.uni-heidelberg.de

## Abstract

Nitric oxide (NO) produced by nitric-oxide synthase (NOS) is a key regulator of animal physiology. Here we uncover a function for NO in the integration of UV exposure and the gating of a UV-avoidance circuit. We studied UV/violet avoidance mediated by brain ciliary photoreceptors (cPRCs) in larvae of the annelid *Platynereis dumerilii*. In the larva, NOS is expressed in interneurons (INNOS) postsynaptic to cPRCs. UV stimulation of cPRCs triggers INNOS activation and NO production. NO signals retrogradely to cPRCs to induce their sustained post-stimulus activation through an unconventional guanylate cyclase. This late activation inhibits serotonergic ciliomotor neurons to induce downward swimming. In *NOS* mutants, retrograde signalling, circuit output and UV avoidance are defective. By mathematical modelling, we recapitulate phototransduction and circuit dynamics in wild-type and mutant larvae. Our results reveal how NO-mediated retrograde signalling gates a synaptic circuit and induces short-term memory of UV exposure to orchestrate light-avoidance behaviour.

## Introduction

In nervous systems, synaptic transmission and volume transmission together shape circuit dynamics (Bargmann and Marder, 2013). While synaptic transmission occurs at specialised contact sites, volume transmission is characterised by the delocalised release of diverse diffusive neuromodulators.

Nitric oxide (NO) is one such modulator with unique physical and signalling properties. This free radical synthesized from L-arginine by nitric oxide synthase (NOS) is short-lived and can diffuse across biological membranes (Cudeiro and Rivadulla, 1999; Thomas, 2015). Canonical NO signalling involves the  $\text{Ca}^{2+}$ /calmodulin-dependent activation of NOS, NO production and diffusion, and the NO-dependent activation of soluble guanylate cyclases (sGC) leading to cGMP production (Bredt et al., 1990; Hölscher, 1997). Given that NOS activation is  $\text{Ca}^{2+}$  dependent and NOS shows neuron-type-specific expression (Aso et al., 2019; Gibbs and Truman, 1998; Mobley et al., 2022; Wildemann and Bicker, 1999), NO action can lead to the activity-dependent modulation of neural circuits at specific sites (Aso et al., 2019; Jacoby et al., 2018; Vielma et al., 2014; Wang et al., 2007).

In the vertebrate retina, NOS is expressed in amacrine, ganglion and other cells and the actions of NO can be diverse (Cudeiro and Rivadulla, 1999; Jacoby et al., 2018; Wang et al., 2007). For example, defective NO signalling in NOS knockout mice leads to a decreased sensitivity of retinal ganglion cells to light stimulation (Wang et al., 2007). In the retina, NO signalling can also involve pathways other than canonical sGC signalling (Jacoby et al., 2018; Tooker et al., 2013; Wei et al., 2012). Due to the complex expression of NOS in vertebrates and the diversity of its functions, it has been challenging to link the neurophysiological effects of NO to signalling mechanisms and behaviour change.

In the *Drosophila* brain, NO signalling is also involved in tuning circuit activity at diverse and specific sites. In the ellipsoid body of the central complex, NO is involved in visual working memory (Kuntz et al., 2017). NO signalling also tunes the dynamics of associative memories in mushroom body circuits. NOS is expressed in PPL1- $\gamma$ 1pedc mushroom-body neurons where it is involved in shortening memory retention while promoting fast memory updating in response to new experiences (Aso et al., 2019).

In the whole organism context, NO signalling has often been studied in diverse marine invertebrates, where NO can regulate larval settlement and metamorphosis (Leise et al., 2001; Locascio et al., 2022; Song et al., 2021; Ueda et al., 2016; Zhang et al., 2012). While NOS-expressing neurons potentially responsible for these effects have been reported (Bishop and Brandhorst, 2007; Locascio et al., 2022), it has not been possible to link these NO-dependent effects on behaviour or life-cycle transitions to neuronal activity and function.

Overall, we still know little about how NO production relates to stimulus conditions, how it shapes circuit activity at specific neuron types, and how NO-dependent modulation relates to behaviour.

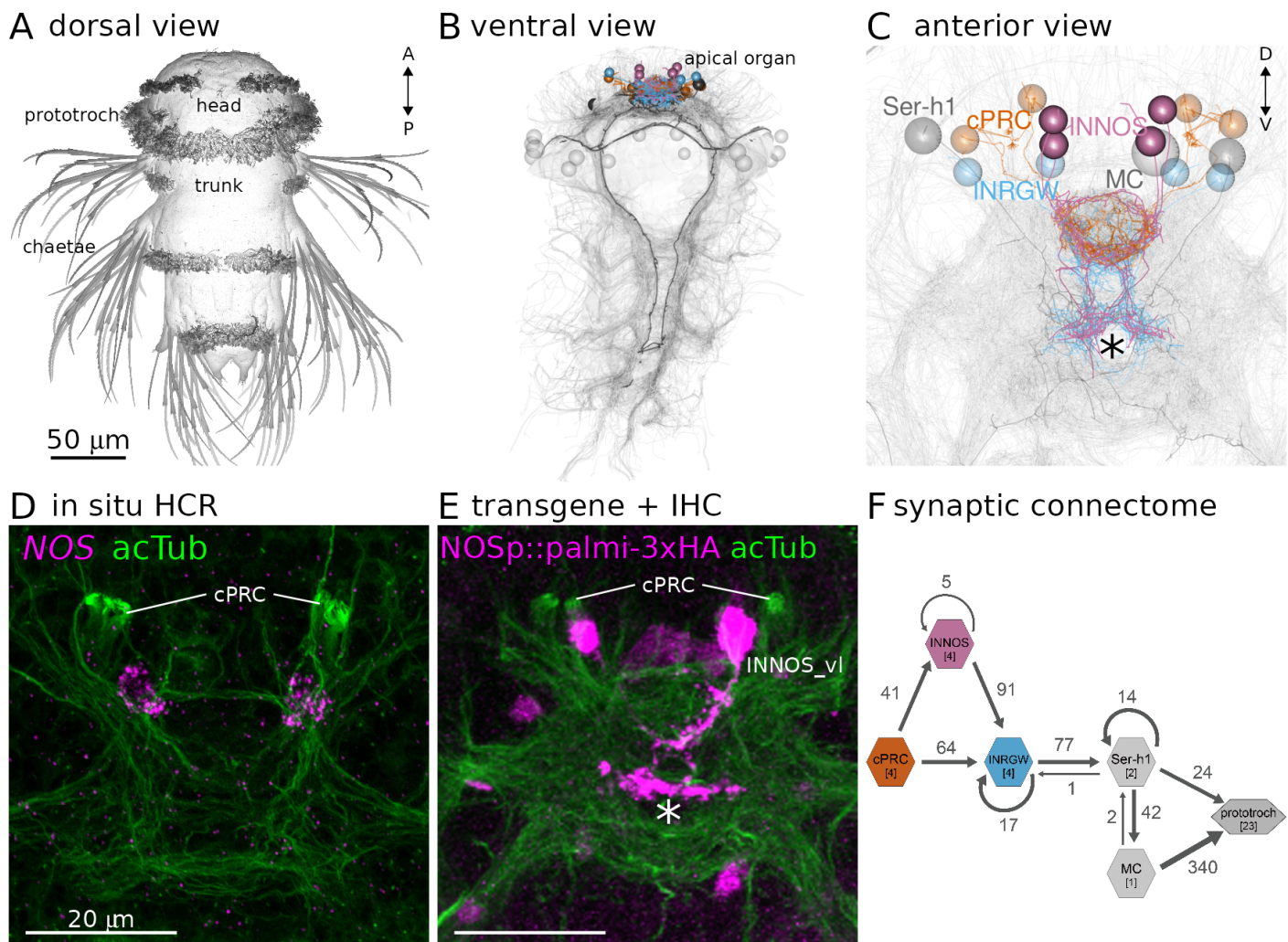
To investigate NO function in neural circuit dynamics and behaviour, here we study larvae of the marine annelid model *Platynereis dumerilii* (Ozpolat et al., 2021). *Platynereis* has emerged as a model for systems neuroscience with a toolkit that enables the combination of behavioural analysis and neuronal activity imaging with genetic manipulations. A whole-body synaptic connectome and gene expression atlases are also available and can be integrated with functional approaches in live animals thanks to the cellular-level stereotypy of larvae of the same developmental stage (Ozpolat et al., 2021; Verasztó et al., 2020; Verasztó et al., 2017; Vergara et al., 2021).

We uncovered an essential function for NO signalling in larval UV/violet-light avoidance behaviour. In *Platynereis* larvae, UV/violet avoidance is mediated by brain ciliary photoreceptor cells (cPRCs) and is characterised by downward swimming (Verasztó et al., 2018). The cPRCs express a ciliary-type opsin, c-opsin1 (Arendt et al., 2004) that forms a UV-absorbing bistable photopigment with an absorption maximum around 384 nm (Tsukamoto et al., 2017; Veedin Rajan et al., 2021; Verasztó et al., 2018). Upon UV/violet exposure, the cPRCs show a characteristic biphasic  $\text{Ca}^{2+}$  response that is c-opsin1 dependent. UV/violet avoidance is also c-opsin1 dependent and is defective in *c-opsin1* mutants (Verasztó et al., 2018). Here we show that *Platynereis* NOS is expressed in interneurons of the cPRC circuit and is required for UV/violet-avoidance. By combining  $\text{Ca}^{2+}$  imaging across the fully-mapped cPRC circuit (Verasztó et al., 2018) with genetic perturbations and mathematical modelling, we describe how NO tunes circuit dynamics through non-synaptic retrograde signalling to cPRCs. This delayed neuroendocrine feedback integrates UV/violet exposure to induce a short-term memory manifested in altered circuit activity and an aversive behavioural response.

## Results

### Nitric oxide synthase is expressed in interneurons of the UV-avoidance circuit

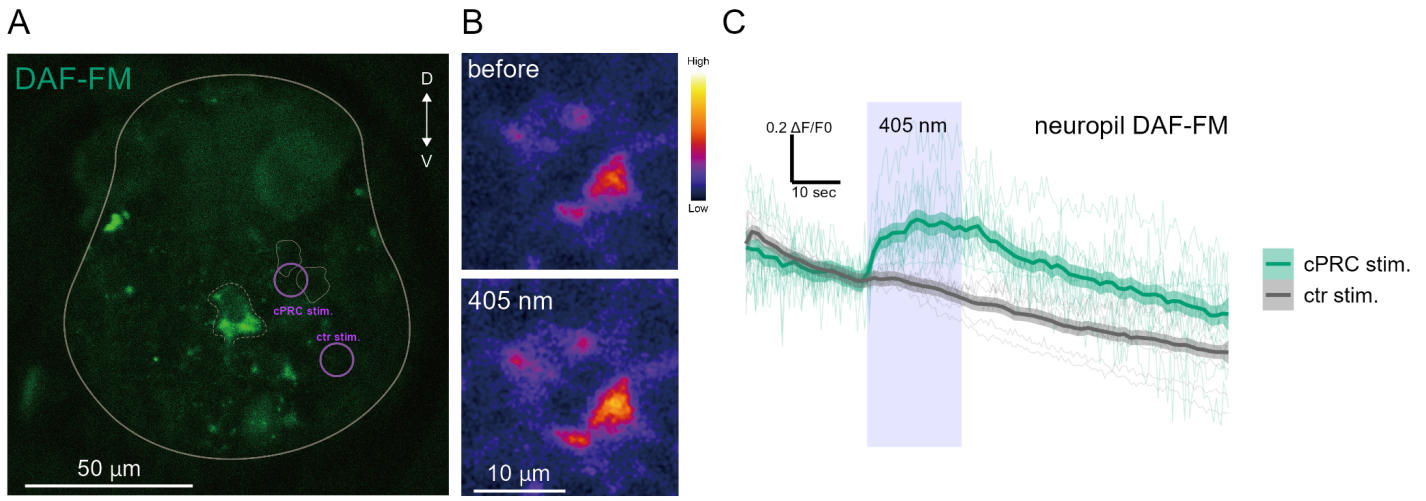
We identified a single *nitric oxide synthase* (*NOS*) gene in the *Platynereis dumerilii* genome and transcriptome data. Phylogenetic analysis of NOS proteins indicate that *Platynereis* NOS belongs to an orthology group of bilaterian NOS sequences (Figure 1—figure supplement 1). To characterise the expression pattern of *NOS*, we used *in situ* hybridization chain reaction (HCR) and transient transgenesis. In two- and three-day-old larvae, we detected *NOS* expression in four cells (two of them weakly expressing) in the apical organ region (Figure 1D and Figure 1—figure supplement 2). *NOS* was also expressed in the region of the visual eyes (adult eyes) and the pigmented eyespots (Figure 1—figure supplement 2). The four apical organ cells, but not the eyes, were also labelled with a *NOS* reporter construct driving palmitoylated tdTomato (Figure 1E). This reporter also revealed the axonal projections of these central NOS-expressing neurons. The position and morphology of the four *NOS*+ cells allowed us to identify the same four cells as four interneurons (INNOS) in our three-day-old whole-body *Platynereis* volume EM data (Verasztó et al., 2020; Williams et al., 2017) (Figure 1B,C). In the synaptic connectome, the INNOS cells are postsynaptic to the UV-sensory cPRCs and presynaptic to the INRGWa interneurons, which are also cPRC targets (Figure 1C, F). The projections of INNOS cells are segregated into input (dendritic) and output (axonal) compartments, with cPRC inputs occurring on the dendritic part in the dense neurosecretory plexus. INNOS output-synapses form in the more ventral projection region (Figure 1—figure supplement 3). INRGWa neurons synapse on the head serotonergic ciliomotor neurons (Ser-h1), which synapse on the cholinergic MC ciliomotor neuron and cells of the prototroch ciliary band (Figure 1C, F) (Verasztó et al., 2017).



**Figure 1. Identification of *NOS*-expressing interneurons (INNOS) within the cPRC circuit.** **(A)** Scanning electron microscopy image of a three-day-old *Platynereis* larva. **(B, C)** Volume rendering of the neuron types (cPRC, INNOS, INRGWa, Ser-h1 and MC) in the cPRC circuit reconstructed from a whole-body transmission electron microscopy volume of a three-day-old larva. Neurite skeletons are shown with cell-body positions represented by spheres. Projections of all neurons in the body are shown in grey to highlight the neuropils. The outline of the yolk is also indicated in grey. In B, nuclei positions of the prototroch head ciliary band are shown as grey spheres. **(D)** Expression of the *NOS* gene detected by in situ HCR (magenta) in a two-day-old larva (anterior view). Antibody staining for acetylated  $\alpha$ -tubulin (acTub: green) highlights cPRC cilia and the neuropil. **(E)** Expression of a *NOS* reporter (*NOSP::palmi-3xHA*; magenta) labelled with an anti-HA antibody in a two-day-old larva (anterior view). Antibody staining for acetylated  $\alpha$ -tubulin (acTub; green) highlights cPRC cilia and the neuropil. **(F)** Synaptic wiring diagram of the cPRC circuit. Hexagons represent cell groups, with the number of cells per group shown in square brackets. Arrows represent the summed number of synaptic contacts between cell groups. Arrow thickness is proportional to the number of synapses.

#### Nitric oxide is produced during UV/violet stimulation of the cPRCs

The expression of *NOS* in the INNOS interneurons in the cPRC circuit suggests that NO signalling may be involved in UV/violet-avoidance. To test this, first we asked whether NO is produced during UV/violet stimulation of the larvae. We injected the fluorescent NO-reporter DAF-FM into zygotes and imaged two-day-old larvae while exposing the region of cPRC cilia to 405 nm violet light. To mark cell outlines, we coinjected mRNA encoding a red-fluorescent reporter (RGECO), allowing the identification of the cPRCs. Following light stimulation in the region of the ramified cilia of the cPRCs, we detected an increase in DAF-FM fluorescence in the anterior neurosecretory neuropil, the region of INNOS projections. This increase did not occur in larvae in which we illuminated a control area (Figure 2).



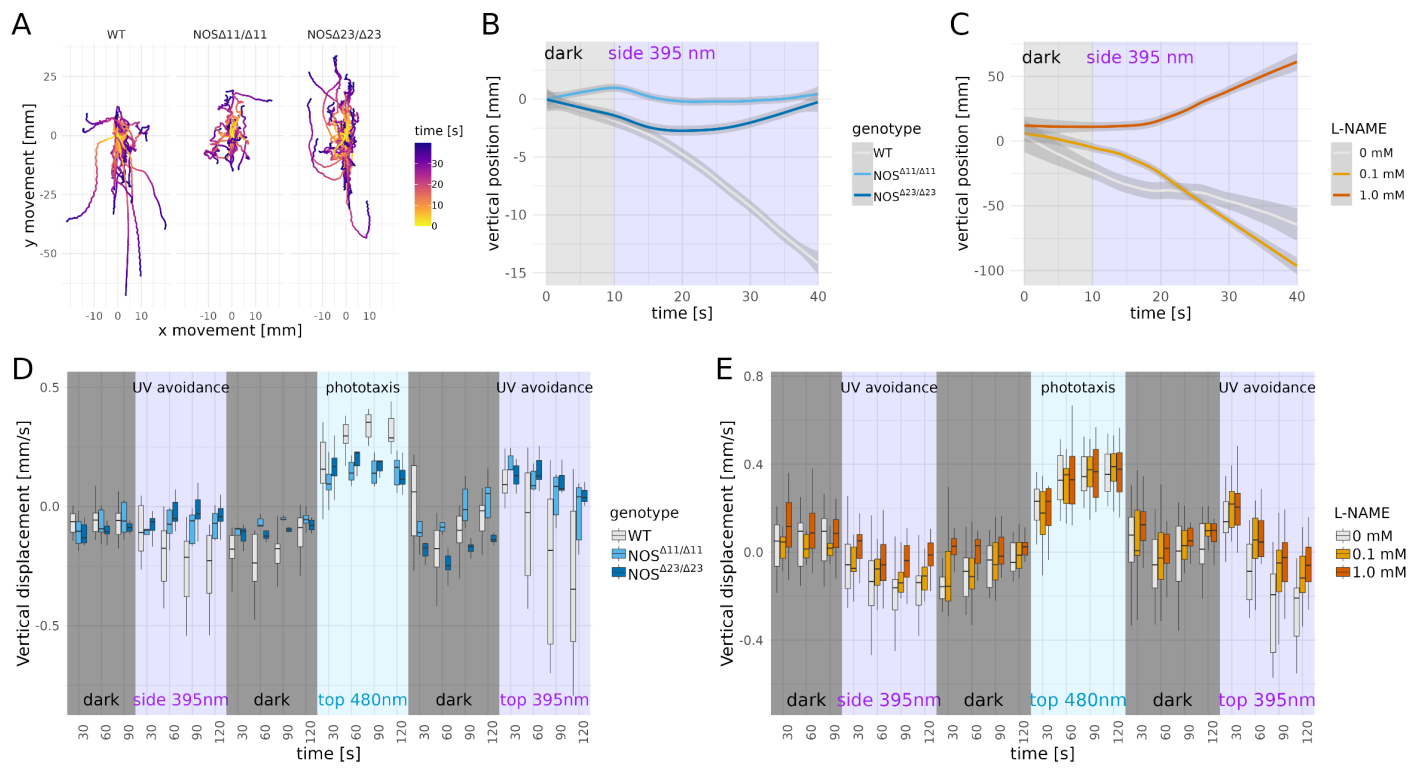
**Figure 2. NO produced by UV/violet stimulation to cPRCs.** (A) DAF-FM fluorescence in the region of the neurosecretory neuropil. The white line indicates the outline of the larva. The dashed line corresponds to the area where fluorescence was quantified. The circles indicate the location of cPRC and control stimulation. The cPRCs are marked by thin lines. (B) DAF-FM fluorescence before and during 405 nm light stimulation. (C) Changes in DAF-FM fluorescence over time during 405 nm stimulation of the cPRCs or a control area (ctr stim.). The purple box indicates the duration of 405 nm stimulation. Individual normalized traces ( $\Delta F/F_0$ ) are shown as thin lines. Thick lines show the mean value with 0.95 confidence intervals. N = 9 larvae for control and 11 for cPRC stimulation.

Figure 2 – source data 1. DAF-FM fluorescence reads.

#### Nitric oxide signalling mediates UV-avoidance behaviour

We next tested whether NO signalling regulates UV/violet avoidance. To achieve this, we generated two *Platynereis* NOS knockout lines using the CRISPR/Cas9 method. We recovered two deletions (NOS $\Delta$ 11/Δ11 and Δ23/Δ23), both frame-shift mutations leading to an early stop codon and thus likely representing null alleles (Figure 3—figure supplement 1A). We could establish a homozygous line for both mutations indicating that NOS is not an essential gene in *Platynereis*. To quantify UV avoidance, we recorded the trajectories of freely swimming wild type and mutant larvae in vertical columns, illuminated laterally from two opposite sides with 395 nm UV light (Figure 3A and Figure 3—figure supplement 1B). As previously shown, wild-type larvae swim downward following non-directional UV/violet light stimulation (Verasztó et al., 2018). In contrast, both two- and three-day-old homozygous NOS-mutant larvae showed a strongly diminished UV-avoidance response (Figure 3A, B and Figure 3—figure supplement 1B, C). This phenotype is similar to the defective UV-avoidance of *c-opsin1* mutant larvae (Verasztó et al., 2018) and reveals a requirement for NOS in UV-avoidance behaviour. Wild type but not mutant larvae also showed an increase in swimming speed under UV light that may be due to downward swimming trajectories (swimming in the direction of gravity) (Figure 3B and Figure 3—figure supplement 1C). We also tested directional phototaxis, by exposing larvae to 480 nm directional collimated light from the top of the column. Three-day-old but not two-day-old NOS-mutant larvae also showed reduced phototactic behaviour, suggesting a function for NOS in the visual eyes that mediate three-day-old phototaxis (Randel et al., 2014) (Figure 3D and Figure 3—figure supplement 1G).

To distinguish between an acute and developmental function of NOS in light responses, we also tested larvae exposed to the NOS inhibitor L-NAME. Larvae incubated for 5 min in 0.1 mM or 1 mM L-NAME showed a dose-dependent inhibition of UV avoidance. In contrast, phototaxis was not affected (Figure 3C, E). Overall, our results indicate an acute requirement for NOS signalling in UV-avoidance and a possible indirect, developmental role in the visual system, reminiscent of the function of NO signalling in *Drosophila* eye development (Gibbs and Truman, 1998).



**Figure 3. NOS is required for UV avoidance in *Platynereis* larvae.** (A) Swimming trajectories of wild type (WT, n=32) and NOS mutant ( $NOS\Delta 11/\Delta 11$ , n=26 and  $NOS\Delta 23/\Delta 23$ , n=47) three-day-old larvae. All trajectories start at 0 x and y position and time 0 corresponding to 10 sec after the onset of 395 nm stimulation from the side. (B) Vertical position of batches of wild type and mutant three-day-old larvae over time under 395 nm UV stimulation. The starting position of each larval trajectory was set to 0. (C) Vertical position of batches of control and L-NAME-treated (0.1 and 1 mM) three-day-old larvae over time under 395 nm UV stimulation. The starting position of each larval trajectory was set to 0. (D) Vertical displacement in 30 sec bins of wild type and mutant ( $NOS\Delta 11/\Delta 11$  and  $NOS\Delta 23/\Delta 23$ ) three-day-old larvae stimulated with 395 nm light from the side, 488 nm light from the top and 395 nm light from the top. (E) Vertical displacement in 30 sec bins of control and L-NAME-treated (0.1 and 1 mM) three-day-old larvae stimulated with 395 nm light from the side, 488 nm light from the top and 395 nm light from the top.

Figure 3 – source data 1-5. Source data for panels A-E.

#### NO retrograde signalling tunes cPRC responses to UV/violet stimulation

To investigate how NO signalling alters the dynamics of the cPRC circuit, we carried out  $\text{Ca}^{2+}$  imaging experiments. We ubiquitously expressed the  $\text{Ca}^{2+}$  sensor GCaMP6s in larvae and imaged  $\text{Ca}^{2+}$  signals during 405 nm stimulation of the cPRCs. As we have shown previously, a 20 sec local stimulation of cPRC cilia led to a transient increase in cPRC  $\text{Ca}^{2+}$  levels, followed by a transient decrease (Verasztó et al., 2018). After ~20-sec,  $\text{Ca}^{2+}$  levels in cPRCs were raising again, reaching higher levels than at the start of the stimulus – a response that may involve cPRC depolarisation (Figure 4A, B). This activation phase occurs after the 20 sec stimulation period and is likely due to a delayed neuroendocrine feedback (Verasztó et al., 2018). To determine whether NO mediates such a feedback, we repeated the experiment in NOS-mutant larvae. While we detected the initial activation phase followed by inhibition, in homozygous NOS-mutants for both CRISPR alleles this was not followed by delayed activation. Instead,  $\text{Ca}^{2+}$  levels dropped to a low steady-state level (Figure 4A, B). We thus identified a requirement for NO signalling in the late-phase activation of cPRCs.

#### Two unconventional guanylate cyclases are expressed in the cPRCs

Next we aimed to identify the NO receptor in the cPRCs. NO generally acts via soluble guanylate cyclases (sGC), belonging to the guanylate cyclase family with a CYC domain (PFAM domain: PF00211). NO binding to the heme group of sGC leads to increased cyclic guanosine monophosphate (cGMP) production. Analysis of sGCs in *Platynereis* indicated that these genes are not expressed in any of the cells of the cPRC circuit (not shown and (Verasztó et al., 2017)). Recently, Moroz and coworkers reported an atypical but widely conserved family of guanylate cyclases with a NIT (nitrite/nitrate sensing) domain (PF08376) (NIT-GC) as potential mediators of NO signalling (Moroz et al., 2020). To identify NIT-GCs in *Platynereis*, we searched transcriptome resources and retrieved 15 potential NIT-GC homologs (Figure 4—figure supplement 1 and 2). To analyse the relationship of these sequences to metazoan NIT-GCs, we retrieved protein sequences with a CYC domain

from the transcriptome and genome databases of 45 metazoan and 2 choanoflagellate species. We carried out cluster analysis and phylogenetic reconstruction on a group of membrane-bound guanylate cyclases with sGCs as an outgroup. In agreement with Moroz et al. (Moroz et al., 2020), we found a group of GCs with NIT domains with representatives in placozoans, cnidarians, some ecdysozoans, echinoderms, and lophotrochozoans. The 15 *Platynereis* sequences belonged to several deeply diverged clades in the phylogenetic tree (Figure 4—figure supplement 1 and 2).

To characterise the expression of NIT-GCs, we used previously published spatially-mapped single-cell transcriptome data (Achim et al., 2015; Williams et al., 2017). Among the 15 NIT-GCs, two showed high and specific expression in the cPRCs and one was expressed in the INNOS cells (Figure 4—figure supplement 2). In the single-cell data, we could identify the cPRCs by the specific expression of the markers *c-opsin1* and the *pedal-peptide2 neuropeptide precursor (MLD proneuropeptide)* (Arendt et al., 2004; Williams et al., 2017) (Figure 4—figure supplement 3A). The INNOS cells were identified by NOS expression and spatial mapping in the brain (Achim et al., 2015). We decided to focus on two NIT-GCs expressed in the cPRCs and with a full-length sequence, *NIT-GC1* and *NIT-GC2*. To confirm the single-cell data, we first carried out *in situ* hybridisation chain reaction (HCR) with probes for *NIT-GC1* and *NIT-GC2* mRNA. Both genes were specifically expressed in the four cPRCs, as confirmed by co-labeling with an acetylated  $\alpha$ -tubulin antibody and with an HCR probe against *pedal peptide 2/MLD proneuropeptide* (Figure 4C, D and Figure 4—figure supplement 3A-C). To analyse the subcellular localisation of NIT-GC1 and NIT-GC2 at the protein level, we raised and affinity-purified polyclonal antibodies against a specific peptide sequence from both proteins. In immunostainings, we found that NIT-GC1 was localised to the region corresponding to the axonal projections of the cPRCs in the anterior neurosecretory plexus (Figure 4E). Co-immunostaining with the rabbit NIT-GC1 antibody and a custom rat antibody raised against *Platynereis* NOS revealed the localisation of both proteins in dots in the neurosecretory neuropil (Figure 4—figure supplement 3D). In contrast, NIT-GC2 specifically labelled the ramified sensory cilia of the cPRCs (Figure 4F). These different subcellular localisations suggest that the two NIT-GCs are involved in different intracellular signalling processes in the ciliary and axonal regions of the cPRCs.

### **NIT-GC1 produces cGMP in an NO-dependent manner**

To further characterise these atypical guanylate cyclases, we focused on NIT-GC1 and carried out *in vitro* experiments. In bacteria, NIT domains are thought to regulate cellular functions in response to intra- or extracellular nitrate and nitrite. NIT-GC1 has a NIT domain and a highly conserved cyclase domain that is expected to catalyse cGMP synthesis (Figure 4G). The NIT domain may render NIT-GC1 dependent on NO signals. To test this, we co-expressed the cGMP indicator Green cGull (Matsuda et al., 2016) and NIT-GC1 in cultured COS-7 (monkey kidney) cells, a cell line with minimal endogenous sGC activity (Matsuda et al., 2016). For balanced expression, we used a single plasmid with the two open-reading frames separated by the 2A self-cleaving peptide (Figure 4H). Application of the NO donor SNAP lead to increased Green cGull fluorescence, an effect we did not observe when cells were exposed to DMSO or when Green cGull was expressed alone (Figure 4I-K). To test whether this effect is dependent on the NIT domain, we also tested a deletion construct of NIT-GC1 lacking the NIT domain (Figure 4G). Cells expressing this construct and Green cGull did not show an increased fluorescence of the cGMP reporter when exposed to SNAP (Figure 4L). These results indicate that NIT-GC1 is able to catalyse cGMP production in an NO-dependent manner and this function requires the NIT domain. These results establish NIT-GC1 as a biochemical sensor of NO or its derivatives.

### **NIT-GC1 is required for NO-mediated retrograde signalling to cPRCs during the UV response**

To test the *in vivo* function of NIT-GC1 and NIT-GC2 in cPRC responses, we combined  $\text{Ca}^{2+}$  imaging with morpholino-mediated knockdowns. We used two translation-blocking morpholinos for each *NIT-GC* gene and tested knockdown efficiency by immunostaining injected animals with the NIT-GC1 and NIT-GC2 antibodies (Figure 4—figure supplement 3E,F). For both genes, the morpholinos led to a strong reduction in the respective antibody signal, confirming efficient knockdown and antibody specificity.

In NIT-GC1 morphant larvae, the delayed activation of cPRCs following 405 nm stimulation did not occur (Figure 4M). This phenotype is similar to the phenotype of *NOS* mutants suggesting that NIT-GC1 acts as the NO sensor in cPRCs to drive their delayed activation. This could occur via increased cGMP production and the opening of a cyclic-nucleotide-gated ion channel (CNG) specific to cPRCs (Tosches et al., 2014). NIT-GC2 morphant larvae, in contrast, showed a step-up increase in  $\text{Ca}^{2+}$  following light stimulation (Figure 4N). The  $\text{Ca}^{2+}$  signal decayed during stimulation and was off after light off. These data support an essential role for ciliary-localised NIT-GC2 in suppressing cPRC  $\text{Ca}^{2+}$  following its transient rise at stimulus onset. Overall, these knockdown experiments revealed different signalling mechanisms for the two NIT-GCs that may be

due to their different subcellular localisations.

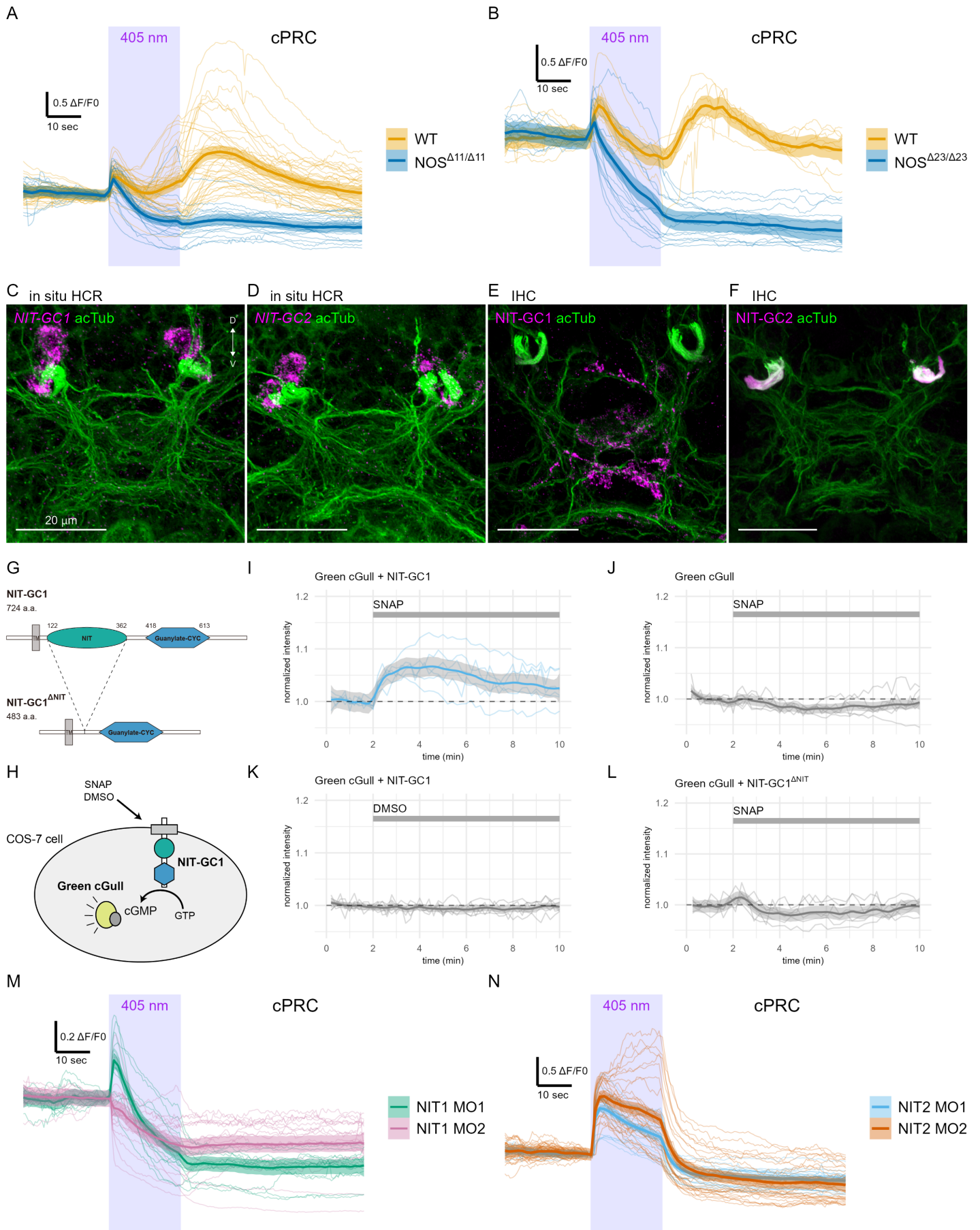


**Figure 4. NOS and two NIT-GCs shape  $\text{Ca}^{2+}$  signals during cPRC UV/violet response. (A, B)** GCaMP6s signals in cPRCs in wild type and NOS mutant (A,  $\text{NOS}\Delta 11/\Delta 11$ , B,  $\text{NOS}\Delta 23/\Delta 23$ ) larvae during 405 nm light stimulation. **(C, D)** In situ HCR for (C) NIT-GC1 and (D) NIT-GC2 (magenta) in three-day-old *Platynereis* larvae. Larvae were co-stained with an antibody against acetylated  $\alpha$ -tubulin to label cPRC cilia and the neuropil (green). **(E, F)** Immunostaining for (E) NIT-GC1 and (F) NIT-GC2 (magenta), co-stained for acetylated  $\alpha$ -tubulin (green). **(G)** The domain structure of *Platynereis* NIT-GC1 and the truncated

NIT-GC1 $\Delta$ NIT protein lacking the NIT domain. A predicted transmembrane region (TM) is shown in grey. (H) Schematic of the cell-based assay to detect cGMP production following the addition of an NO donor SNAP or DMSO as control. (I-L) Green cGull fluorescence over time for the four conditions tested. Individual responses and their mean with 0.95 confidence interval are shown ( $n > 6$  cells). Intensities are normalized ( $\Delta F/F_0$ ). The indicated chemicals were added at 2 min after the start of imaging (grey bars). (M, N) GCaMP6s signals in cPRCs in (M) NIT-GC1 and (N) NIT-GC2 morphant larvae during 405 nm light stimulation. Individual responses and their mean with 0.95 confidence interval are shown.

Figure 4 – source data 1-8. Source data for panels A, B and I-N.

### NO signalling shapes the dynamics of the cPRC circuit

To investigate how NO and NIT-GC signalling influence the dynamics of the cPRC circuit, we imaged  $\text{Ca}^{2+}$  signals from postsynaptic neurons in wild type, mutant and morphant larvae. We were able to image the activity of all neurons in the cPRC circuit (INNOS, INRGWa, Ser-h1 and MC). The MC cell was identified based on its position and intrinsic activity (Verasztó et al., 2017). To unambiguously identify all other cells from which we recorded  $\text{Ca}^{2+}$  signals, we developed an on-slide immunostaining method (Figure 5—figure supplement 1A). We used the cell-specific antibody markers against RYamide (INNOS) (Figure 5—figure supplement 1B-D), RGWamide (INRGWa) and serotonin (Ser-h1) (Conzelmann et al., 2011) to immunostain agar-embedded larvae following  $\text{Ca}^{2+}$  imaging. Based on the position of the nuclei, we could correlate live and fixed samples at a single-cell precision (Figure 5A, B). Due to the stereotypy of the larvae, we could also identify neurons based on their position and  $\text{Ca}^{2+}$  activity in activity-correlation maps (Figure 5C).

We first quantified the responses of the INNOS and INRGWa interneurons during 405 nm stimulation of the cPRCs. In both wild type and *NOS*-mutant larvae, INNOS cells showed an increase in  $\text{Ca}^{2+}$  during stimulation (Figure 5D). In contrast, the INNOS response was flat or slightly negative in NIT-GC2 morphant larvae (Figure 5E) revealing an essential role for NIT-GC2-mediated cPRC suppression in INNOS activation. The INRGWa cells were initially inhibited during cPRC stimulation, followed by a delayed activation paralleling the second activation phase of the cPRCs. This late INRGWa response was lacking in *NOS*-mutants (Figure 5F). In NIT-GC2 morphants, INRGWa cells showed a transient increase in  $\text{Ca}^{2+}$  that decayed after light off and a delayed activation was not present (Figure 5G).

Next, we imaged  $\text{Ca}^{2+}$  signals from Ser-h1 and MC neurons in wild type and *NOS* mutant larvae. Ser-h1 cells showed an activation profile that correlated with cPRC activity, including a reduction in  $\text{Ca}^{2+}$  during stimulation followed by a rebound, a response that was defective in *NOS* mutants (Figure 5I). The MC cell showed sustained activation, including a late-phase that was lacking in *NOS* mutants (Figure 5J). These data suggest that during 405 nm stimulation the Ser-h1 cells are inhibited and the MC cell is activated, and this regulation is NO-dependent. This pattern is expected to inhibit ciliary activity in the prototroch but not in the other ciliary bands (with no Ser-h1 or MC synapses), triggering NO-dependent downward swimming.

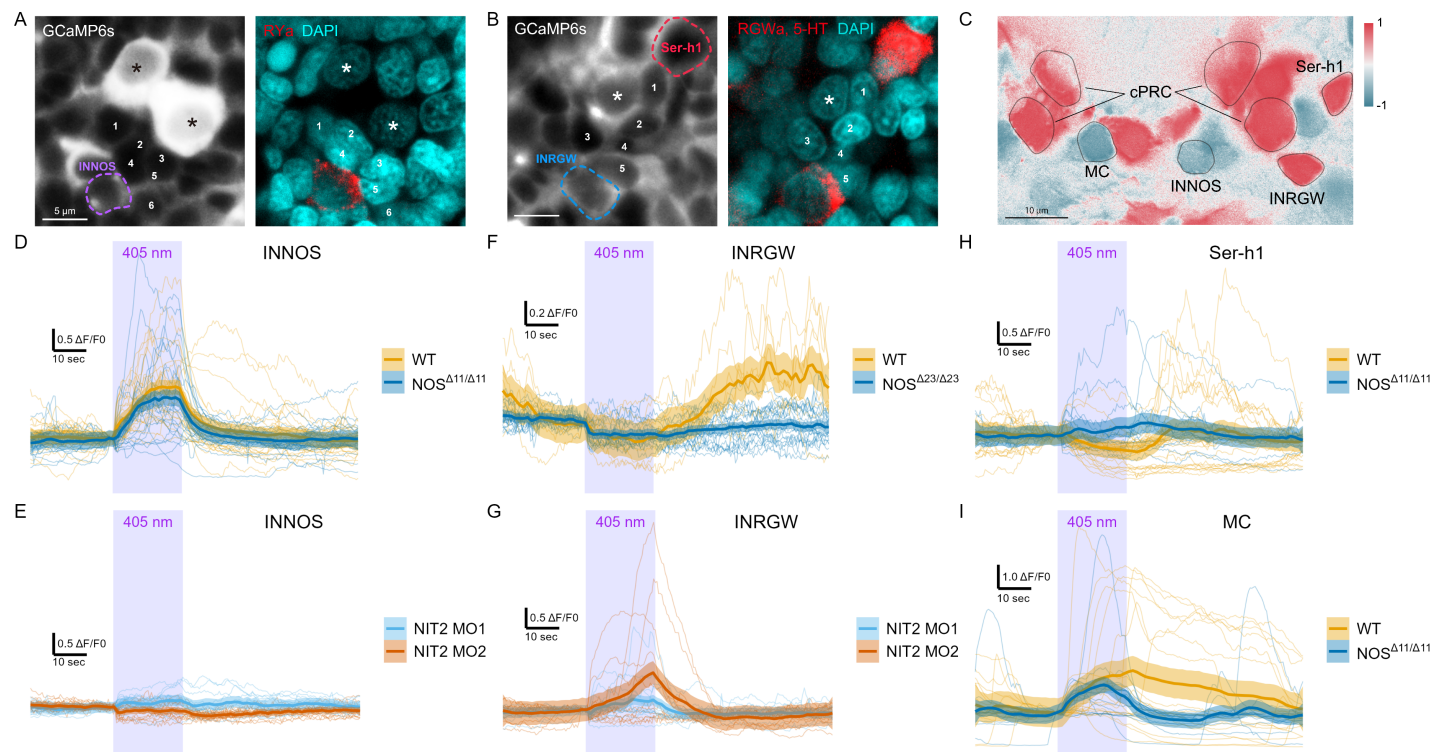


**Figure 5. NOS- and NIT-GC2-dependent dynamics of the cPRC circuit.** (A, B) GCaMP6s imaging from cPRCs and INNOS cells (left panels) followed by on-slide immunostaining for (A) RYamide to label INNOS and (B) RGWamide+serotonin to label INRGWa and Ser-h1 (red). Nuclei are stained with DAPI (cyan). Asterisks indicate cPRC nuclei. Numbers mark the same cells in the GCaMP and immunostaining images matched by position. (C) Correlation map of neuronal activity of the cPRCs, INNOS, INRGWa, Ser-h1 and MC neurons. (D) GCaMP6s fluorescence in INNOS cells in wild type (WT) and *NOSΔ11/Δ11* mutant larvae during 405 nm stimulation of the cPRC cilia. (E) GCaMP6s fluorescence in INNOS cells in NIT-GC2 morphant larvae during 405 nm stimulation. (F) GCaMP6s fluorescence in INRGWa cells in wild type and *NOSΔ23/Δ23* mutant larvae during 405 nm stimulation. (G) GCaMP6s fluorescence in INRGWa cells in NIT-GC2 morphant larvae during 405 nm stimulation. (H, I) GCaMP6s fluorescence in (H) Ser-h1 cells and (I) the MC cell in wild type and *NOSΔ11/Δ11* mutant larvae during 405 nm stimulation.

Figure 5 – source data 1-6. Source data for panels D-I.

### Mathematical modelling of cPRC-circuit dynamics

To further analyse the dynamics of responses to UV light and formally describe cPRC phototransduction, synaptic connections and NO retrograde signalling, we developed a mixed cellular-circuit-level mathematical model. We used our  $\text{Ca}^{2+}$  imaging data of cPRC, INNOS and INRGWa cells collected in wild type, *NOS* knockout and *NIT-GC2* morphant larvae to formulate assumptions that are the basis of the proposed model.

We modeled a direct c-opsin1-dependent response to UV leading to the initial rise in  $\text{Ca}^{2+}$  levels. The mechanism of this signal is not known but may include  $G\alpha$  and  $G\beta$  signalling, CNGA $\alpha$  channel activation or other pathways. We further assumed that in cPRC cells,  $\text{Ca}^{2+}$  levels increase with cGMP. We modeled a decrease in cGMP and  $\text{Ca}^{2+}$  levels due to a NIT-GC2-dependent pathway (Figure 6A). The effect of NO in cPRC cells is captured by another term that describes a NIT-GC1 and NO-dependent increase in cGMP. Based on the synaptic connectome, we inferred a feedforward coupling between cPRC cells and INNOS and INRGWa cells. The proposed synaptic coupling is UV-dependent, decays linearly and is suppressed in NIT-GC2 morphants (Figure 6A).

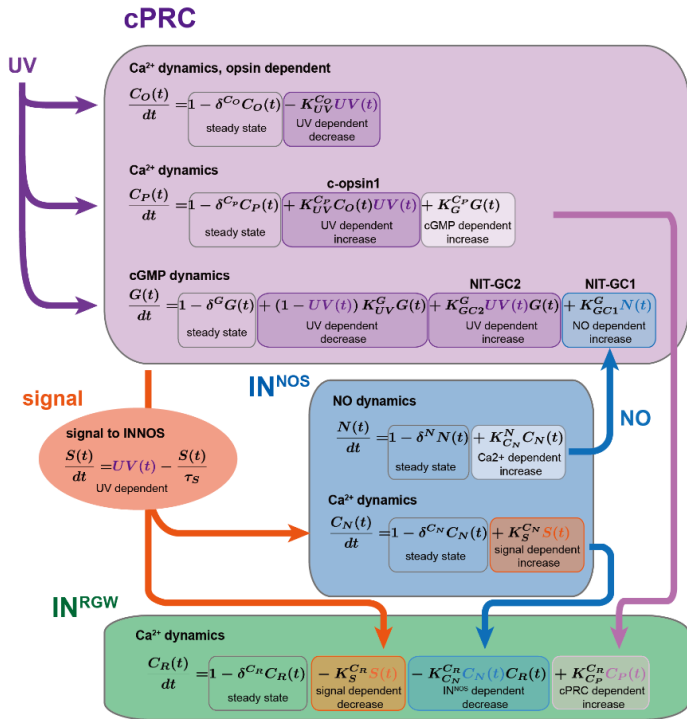
In the INNOS cells, we assumed that excitatory synaptic input from cPRC (or rebound from tonic inhibition) leads to a rise in  $\text{Ca}^{2+}$  leading to NO production via NOS. This input is NIT-GC2-dependent. In the INRGWa cells, we modeled a decrease in  $\text{Ca}^{2+}$  based on an inhibitory UV-dependent synaptic signal from the cPRCs. We further assumed the existence of direct excitatory coupling between cPRC  $\text{Ca}^{2+}$  levels and INRGWa  $\text{Ca}^{2+}$  to account for the late effects of cPRC on INRGWa (Figure 6A). The UV-dependent and  $\text{Ca}^{2+}$ -dependent signals may be mediated by different transmitters released by cPRCs during distinct phases of their activation cycle. In addition, we assumed a direct inhibitory coupling between INNOS  $\text{Ca}^{2+}$  and INRGWa  $\text{Ca}^{2+}$ . Finally, in all variables, we assumed a linear decay and constant production to set a steady state (Figure 6A). Since the aim of the model is to capture the normalised fluorescence data, the model is nondimensionalised. UV stimulation is modelled as a square pulse. To find model parameters producing an output fitting the experimental data we employed a global optimisation method known as a genetic algorithm (GA).

Through this optimisation procedure, we found parameters that gave a fit to our experimental data under all conditions (Figure 6B; Figure 6-figure supplement 1-5). We could fit to mean  $\text{Ca}^{2+}$  profiles but also individual  $\text{Ca}^{2+}$  transients. Our model only includes a minimal set of parameters and assumptions of interactions that are required to describe the dynamics of cPRC, INNOS and INRGWa in wild type and loss-of-function conditions (Figure 6A, B). The model highlights that cPRC phototransduction employs distinct pathways that operate on different time scales and differentially influence cPRC  $\text{Ca}^{2+}$  levels. The coupling between cPRCs and interneurons also requires different signalling mechanisms, either through distinct neurotransmitters or receptors expressed in the different cells.

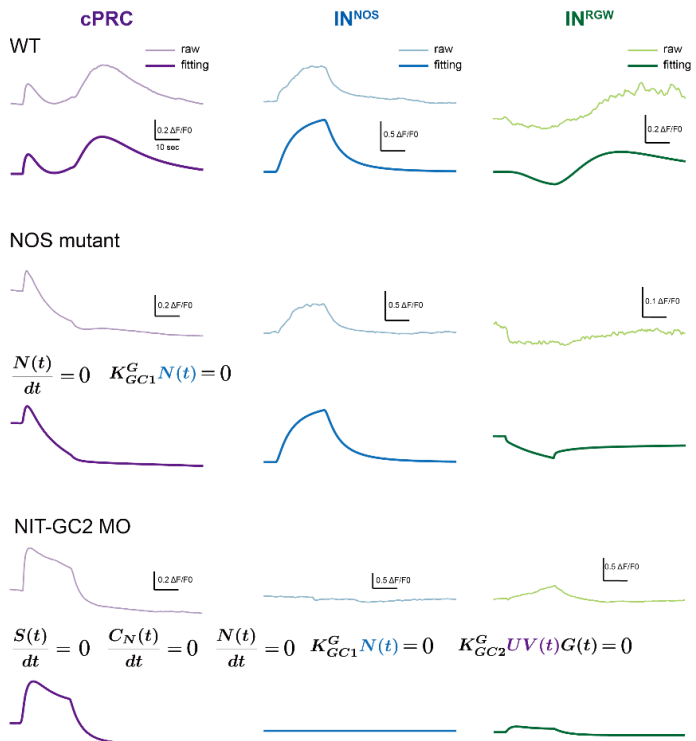
To identify possible molecular pathways, we analysed single-cell transcriptome data for cPRC, INNOS and INRGWa identified by spatial mapping (Achim et al., 2015) and unique marker genes (Williams et al., 2017). In cPRCs, we found transporters and synthetic enzymes indicating cholinergic, glutaminergic, glycinergic, GABAergic and adrenergic neurotransmission (Figure 6C). For each neurotransmitter, we also found receptor-encoding genes expressed in INNOS and INRGWa (Figure 6C). The two types of interneurons often expressed different subunits or types of these receptors, indicating differential signalling (Figure 6C).

Based on these data, our experimental results and the mathematical model, we assembled a minimal phototransduction and circuit diagram. The components for which experimental data are available are shown in bold. Other potential molecular players are also indicated (Figure 6D).

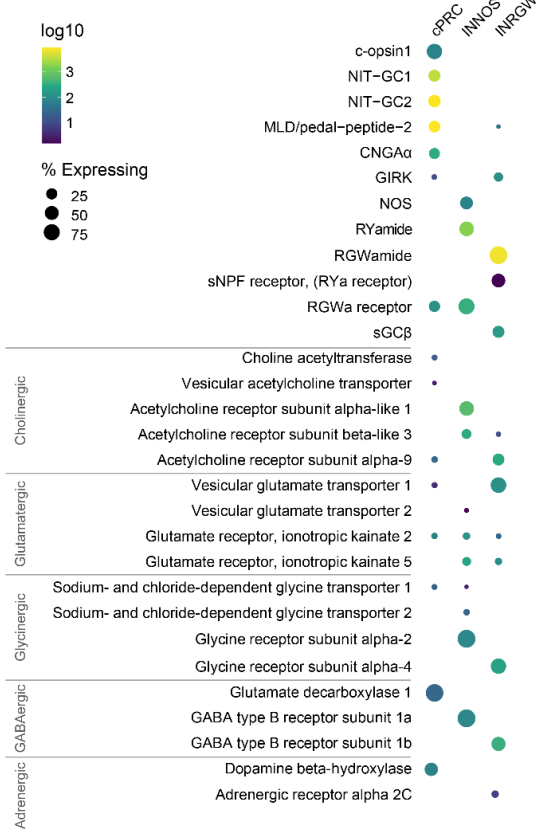
A



B



C



D

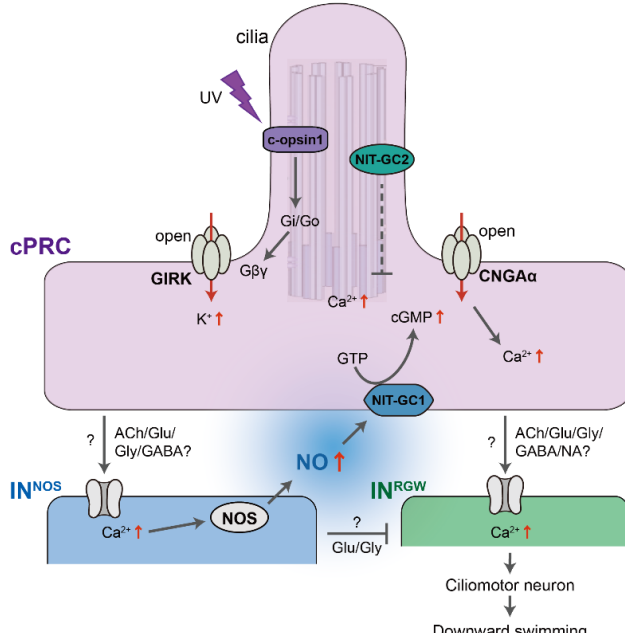


**Figure 6. Mathematical modelling and signalling mechanisms of the cPRC circuit.** (A) Diagram of the mathematical model with the components, interactions, parameters and equations used to model Ca<sup>2+</sup> dynamics. (B) Average Ca<sup>2+</sup> traces (upper) and traces from model simulations (lower) fitted to the data. (C) Dot plot of genes (columns) expressed in three types of cells (rows) in the cPRC circuit using single cell RNA-Seq. The size of the dots is expressed in proportion to the percentage of cells expressing that gene relative to all cells. The colours represent the normal logarithm of the number of transcripts in the cells expressing the gene. (D) Schematic diagram of the signalling pathway of the cPRC circuit, focusing on the NO feedback.

Figure 6 – source data 1. TPM values for each gene and the percentage of expressed genes.

To generate new insights from the model, we asked how the duration and intensity of UV stimulation influences signalling output, measured as the magnitude (quantified as area under peak, AUP) of the NO-dependent  $\text{Ca}^{2+}$  signal in the cPRCs. The model allowed us to systematically vary stimulus conditions that would not have been feasible in single-larva experiments. We found that delayed activation occurs only for UV stimulation of sufficient amplitude and duration (Figure 7). This suggests an integratory function of NO signalling to tune circuit output to the strength of UV exposure.

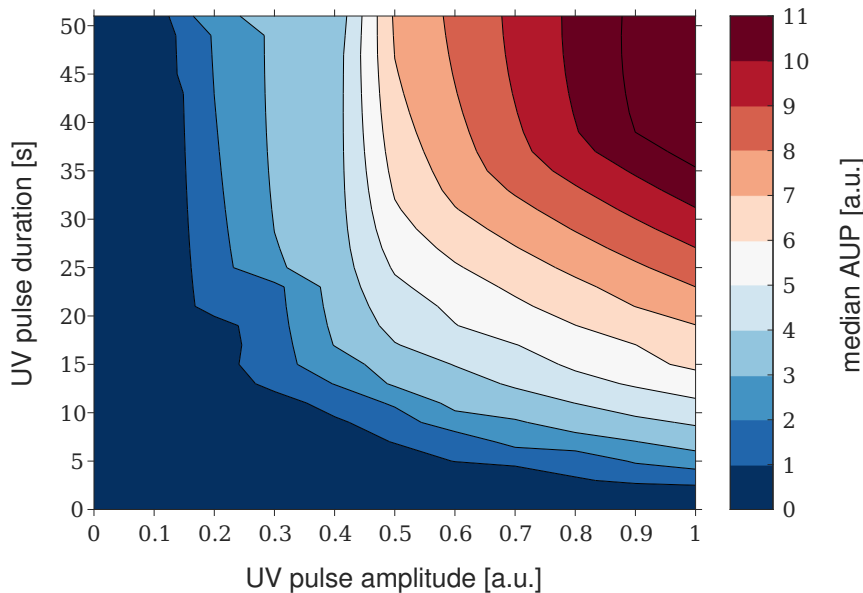


**Figure 7. Magnitude of cPRC activation as a function of stimulus duration and intensity.** Median values of the  $AUP$  are presented as a heatmap with dark blue indicating flat  $C_P(t)$  traces with median  $AUP$  close to 0 and red indicating that the  $C_P(t)$  traces have a clearly defined delayed activation peak.

## Discussion

Our work revealed an essential role for NO-mediated signalling in driving UV/violet avoidance behaviour in larval *Platynereis*. NO, produced by postsynaptic INNOS interneurons, signals retrogradely to presynaptic cPRCs via NIT-GC1 leading to delayed and sustained cPRC activation. This late-phase activation of the photoreceptors drives circuit output through projection interneurons and ciliomotor neurons. In the cPRC circuit, synaptic connectivity alone is thus not sufficient to account for circuit dynamics and behavioural change, as documented in other circuits (Bargmann and Marder, 2013; Imambocus et al., 2022).

### Localised NO signalling in the neurosecretory plexus

NO is a free radical with a millisecond-to-second half life and thus a limited signalling range. In neuronal signalling, NOS is often localised to neurites (Kuntz et al., 2017) close to sGC at synapses (Burette et al., 2002; Garthwaite, 2015). In the cPRC circuit, NOS is localised to the dendritic compartment of INNOS cells where also cPRC postsynaptic sites occur. NIT-GC1, the target of NO signalling is localised to cPRC projections. NO-mediated retrograde signalling thus likely occurs in the neurosecretory plexus where NOS- and NIT-GC1-containing projections are in close proximity and where we detected NO production after UV stimulation. In contrast, INNOS to INRGWa synapses occur outside the neurosecretory plexus in the ventral brain neuropil.

Compartmentalised signalling also occurs in peptidergic modulatory systems and can enable selective network activity during specific behaviours. In the UV-avoidance circuit of *Drosophila* larvae, a peptidergic hub neuron Dp7 links UV-sensory neurons (v'td2) and motor circuits. Dp7 expresses an insulin-like peptide Ilp7 that is required for acute and sustained UV avoidance. Ilp7 signalling occurs at a functionally and morphologically distinct dendritic compartment of Dp7, segregated from other sensory-motor pathways involving Dp7 (Imambocus et al., 2022).

### Functional diversity of NIT-GCs

NO signalling is commonly mediated by sGCs. We identified 12 sGCs in *Platynereis*, but none of these is expressed in the cPRC based on the available scRNASeq data. Instead, we identified an unconventional cPRC-expressed NIT-domain containing GC, NIT-GC1 as the mediator of NO retrograde signalling. In an in vitro assay, we could show that NIT-GC1 can

produce cGMP following the addition of an NO donor and that this activity requires the NIT domain.

NIT domains were first identified in bacteria and animal NIT-GCs have only recently been reported (Moroz et al., 2020; Shu et al., 2003). Bacterial NIT domains regulate cellular functions in response to changes in extracellular and intracellular nitrate and/or nitrite concentrations (Camargo et al., 2007). NO is readily converted to nitrate and nitrite (Garthwaite, 2015; Möller et al., 2019; Santos et al., 2011) and these molecules accumulate in placozoans and cnidarians in cells and tissues with high NOS activity (Moroz et al., 2020, 2004). NIT domains in NIT-GCs may also sense nitrate and nitrite, as in bacteria, a possibility we cannot rule out based on our cellular assays with NIT-GC1. If different NIT-GCs have different sensitivities to NO, nitrite and nitrate, then a range of activation timings may be possible due to the different half-lives of these molecules (Lundberg et al., 2011).

NIT-GC1 and NIT-GC2 showed specific cellular co-expression but very different subcellular localisation and function. In *Platynereis*, we identified 15 NIT-GCs, suggesting a wide range of functions. Differences in subcellular localisation and biochemical function thus seem to also contribute to the diversity of NIT-GC functions in addition to differences in expression.

### Mechanism of phototransduction and neurotransmission in the cPRC circuit

Based on our data herein and previous work we can now propose a more detailed model of cPRC phototransduction and neurotransmission. The cPRCs have high basal  $\text{Ca}^{2+}$  and respond to UV/violet light dependent on c-opsin1 (Verasztó et al., 2018). c-opsin1 forms a bistable photopigment and signals through  $\text{G}\alpha_i$  and  $\text{G}\beta\gamma$  (Tsukamoto et al., 2017; Tsukamoto and Kubo, 2023; Veedin Rajan et al., 2021). In heterologous systems, the  $\text{G}\beta\gamma$  subunits released following c-opsin1 activation open GIRK channels inducing  $\text{K}^+$  efflux (hyperpolarisation) (Tsukamoto et al., 2017; Tsukamoto and Kubo, 2023) and close voltage-gated  $\text{Ca}^{2+}$  channels, thereby reducing intracellular  $\text{Ca}^{2+}$  levels (Tsukamoto and Kubo, 2023). A GIRK channel is also expressed in the cPRCs (Figure 6A). The pathway for the first rapid cPRC activation phase following UV/violet stimulus is not known but may involve the activation of a CNG $\alpha$  channel expressed in the cPRCs (Tosches et al., 2014). For the second inhibitory phase of phototransduction, we identified a key requirement for ciliary-localised NIT-GC2. The mechanisms may involve c-opsin1-dependent inhibition of tonic NIT-GC2 activity and the reduction of ciliary cGMP.

NIT-GC2-dependent signalling is required for the feedforward activation of the INNOS cells through an unknown transmitter. The activation of INNOS leads to NOS activation and NO release, potentially through a canonical  $\text{Ca}^{2+}$ -calmodulin pathway. Our model predicts feedforward inhibition from INNOS to INRGWa, possibly mediated by glycine transmission. NO released by INNOS neurites activates NIT-GC1 in cPRC projections that could lead to cGMP production and the opening of CNG $\alpha$ . This late-phase cPRC activation does not directly depend on the UV/violet signal and can happen post-stimulus. The late-phase cPRC activation leads to INRGWa activation via an unknown transmitter that is likely different from the one acting on INNOS.

In addition, the cPRC circuit expresses several neuropeptides and their receptors, suggesting further neuromodulatory signals. For example, the INRGWa cells express the proneuropeptide RGWamide and cPRCs and INNOS express its receptor, suggesting retrograde peptidergic signalling in the circuit.

We have recently shown that the cPRC circuit also mediates responses to hydrostatic pressure via the same motor system involving Ser-h1 and the prototroch ciliary band. Increased pressure induces cPRC activation and a circuit output that is inverted relative to UV-induced activation. Consequently, ciliary beating increases and the larvae swim upwards. The effect of pressure on cilia requires synaptic transmission by the serotonergic Ser-h1 neurons (Bezares-Calderón et al., 2023).

Pressure-induced  $\text{Ca}^{2+}$  transients in cPRCs lack an inhibitory phase and late activation and resemble UV responses in NIT-GC2 morphants (Bezares-Calderón et al., 2023). This indicates that the differentiation of sensory cues by the multisensory cPRCs occurs already at the level of sensory signal transduction. The different signalling pathways then likely result in the differential release of transmitters and modulators that are decoded by the postsynaptic interneuron circuit. The complex transmitter phenotype of cPRCs could underlie such differential signal processing.

### Nitric oxide confers short-term memory to circuit activity

Retrograde signalling by NO from INNOS to cPRC leads to the sustained activation of cPRCs and postsynaptic neurons even after the end of stimulation. This activated state is maintained for several tens of seconds. NO signalling thus induces a transient circuit state or short-term memory trace in the *Platynereis* larval brain. Because of the short life time of NO, this

molecule may be well suited to encode transient memory traces (Kuntz et al., 2017).

In the ellipsoid body of the *Drosophila* central brain, NO signalling has a similar function. Here, NOS is specifically expressed in the R3 ring neurons and is required for the short-term (~4 sec) visual memory of objects (Kuntz et al., 2017). NO is produced in the axons of R3 neurons and acts directly on sGC in the same axons. This autocrine signal leads to a CNG-dependent temporary increase in  $\text{Ca}^{2+}$  levels, carrying the working memory trace (Kuntz et al., 2017).

In the *Platynereis* circuit, our mathematical model indicates that the magnitude of the NO-dependent signal depends on the intensity and duration of the UV/violet stimulus. This suggests that the NO-dependent memory trace also encodes the intensity and duration of the stimulus.

During UV avoidance in the planarian *Schmidtea mediterranea*, neuropeptide signalling has a similar integratory function. Planarians exposed to UV light for >30 sec remain active for extended periods (several minutes) post-stimulation (Bray et al., 2023). If neuropeptide signalling is defective, animals can still respond to UV light, but do not maintain a latent memory state and do not display increased post-stimulus activity.

### The possible mechanism of UV-induced downward swimming

Non-directional UV/violet light induces downward swimming head down in *Platynereis* larvae (Verasztó et al., 2018). Since stimulus direction is not relevant, swimming direction must be determined by gravity.

Connectome reconstruction and whole-body cell annotation in the three-day-old *Platynereis* larva has not revealed any balancer organ to sense orientation in the gravity field (Bezares-Calderón et al., 2019; Verasztó et al., 2020). It follows that body orientation must be determined by physical parameters including the buoyancy, centre of mass and shape of the larva as well as differential ciliary activity. Except for ciliary activity, all these parameters are likely invariant during the UV response. Our data suggest the UV-dependent inhibition of prototroch ciliary beating via Ser-h1 inhibition and MC activation (Verasztó et al., 2017).

We hypothesize that the differential beating of prototroch versus trunk cilia causes a head-up or head-down orientation due to physics alone. During the UV response, prototroch cilia beat slower than trunk cilia, resulting in a head-down stable state ('rear-wheel drive'). In contrast, during the pressure response prototroch cilia beat faster than trunk cilia (Bezares-Calderón et al., 2023), leading to a head-up orientation ('front-wheel drive'). Testing this hypothesis will require biophysical experiments and mathematical modelling.

### UV-avoidance circuits of extraocular photoreceptors

Animals evolved distinct photosensory systems coupled to non-overlapping circuits and guiding unique behavioural responses. These sensory systems can employ different opsin molecules and be tuned to different wavelengths of light. The avoidance of noxious UV/violet light is often mediated by extraocular photoreceptors and their circuits, distinct from the pigmented visual eyes. These two types of systems co-exist in *Platynereis* where the pigmented eyes and eyespots guide phototaxis with a maximum sensitivity to cyan light (~500 nm) (Gühmann et al., 2015; Randel et al., 2014; Verasztó et al., 2018). Planarians also have pigmented visual eyes mediating phototaxis to cyan light and peripheral extraocular photoreceptors mediating UV avoidance behaviour (Shettigar et al., 2021). *Drosophila* larvae have cerebral eyes called Bolwig's organs involved in phototaxis (Kane et al., 2013) and several types of extraocular UV-sensory cells that tile the body wall and mediate UV avoidance (Imambocus et al., 2022).

One common feature of UV-avoidance circuits is their sustained post-stimulus activation following UV exposure. This can involve peptidergic signals as in planaria and maggots (Bray et al., 2023; Imambocus et al., 2022) or NO as in *Platynereis*. Volume transmission is well suited to integrate light exposure and maintain an internal state following noxious stimulation. The amount of modulator released can scale with stimulus intensity or duration and maintain an altered circuit state due to the slower decay of the diffusive signals relative to synaptic transmission.

Overall, we have revealed how NO shapes the dynamics of a fully mapped sensory-motor UV avoidance circuit. We identified an unconventional GC as the NO receptor and measured circuit activity in different genetic backgrounds. Finally, we could link circuit activity to light-avoidance behaviour. The richly modulated multi-transmitter cPRC circuit will serve as a fertile ground for future studies on how neuromodulators shape activity and behaviour.

## Key resources table

Reagent type (species)	Designation	Source or reference	Identifiers	Additional information
Strain ( <i>Platynereis dumerilii</i> )	NOSΔ11/Δ11 knockout	This paper		Knockout generated
Strain ( <i>Platynereis dumerilii</i> )	NOSΔ23/Δ23 knockout	This paper		Knockout generated
Strain ( <i>Platynereis dumerilii</i> )	NOSΔ11/Δ23 knockout	This paper		Knockout generated
Cell line ( <i>Cercopithecus aethiops</i> )	COS-7 cell	<a href="https://www.atcc.org/products/crl-1651">https://www.atcc.org /products/crl-1651</a> ( <a href="https://www.atcc.org/products/crl-1651">https://www.atcc.org /products/crl-1651</a> ).	RRID:CVCL_0224	ATCC (CRL-1651™)
Biological sample ( <i>Platynereis dumerilii</i> )	Wild type Tübingen strain	Other	NCBITaxon:6359	Jékely lab strain (Tübingen)
Gene ( <i>Platynereis dumerilii</i> )	NOS	This paper	GenBank_Acc#:	
Gene ( <i>Platynereis dumerilii</i> )	NIT-GC1	This paper	GenBank_Acc#:	
Gene ( <i>Platynereis dumerilii</i> )	NIT-GC2	This paper	GenBank_Acc#:	
NOS: Nitric_Oxide_Synthase	To amplify Promoter & Regulatory region	Fwd	NOSProm2ndF0.6BamHIAGGGATCCCCAATGCG	
NOS: Nitric_Oxide_Synthase	To amplify Promoter & Regulatory region	Rev	GeR1ASCI	AAGGCGCGCCCCACC
NOS: Nitric_Oxide_Synthase	Mutation Check on Exon3	Fwd		Exon3 Sequence F-27bp GGTCATTGGTTTCG/
NOS: Nitric_Oxide_Synthase	Mutation Check on Exon3	Rev		Exon3 Sequence R-27bp CAGAGTCGATCAGTC/
NOS: Nitric_Oxide_Synthase	Sequencing primer for Exon3 mutation check	Fwd	Exon3 Sequence F-2	GGTGCTCTCCGGGT/
RNA	sgRNA			5'-TAGGGCAATACTGC
RNA	sgRNA			5'-AAACGAGTGGAGC
RNA	pUC57-T7-RPP2-hSpCas9-HA-2XNLS-GFP		plasmid	Bezares-Calderón et al.
Antibody	Monoclonal Anti-Tubulin, Acetylated antibody	Sigma-Aldrich	Cat#:T6793, RRID:AB_477585	
Antibody	HA-Tag (C29F4), Rabbit mAb	Cell Signaling Technology	Cat#:3724P	
NIT-GC1 polyclonal antibody	CYWLLGRKERRPKRRL-amide	This paper	rabbit	Altabioscience
NIT-GC2 polyclonal antibody	CTEGSTKEGKKEGQ-amide	This paper	rabbit	Altabioscience
NOS polyclonal antibody	CKPSYELQDPWKTYIWRKD-amide	This paper	Rat	Altabioscience
Antibody	RYamide neuropeptide antibody	CRY-amide	rabbit	Conzelmann and Jékely
Antibody	RGWamide neuropeptide antibody	CGW-amide	rabbit	Conzelmann and Jékely

Reagent type (species)	Designation	Source or reference	Identifiers	Additional information
Antibody	F(ab')2-Goat anti-Rabbit IgG (H+L) Cross-Adsorbed Secondary Antibody, Alexa Fluor™ 546 Goat anti-Rat IgG (H+L)	Invitrogen	Catalog # A-11071	
Antibody	Highly Cross-Adsorbed Secondary Antibody, Alexa Fluor™ Plus 594 F(ab')2-Goat anti-Mouse IgG (H+L) Cross-Adsorbed Secondary Antibody, Alexa Fluor™ 647	Invitrogen	Catalog # A48264	
Antibody	NIT-GC1 full	comp411593_c0_seq1_309_F	Catalog # A-21237	GGTTGAATAATGACAA
Recombinant DNA reagent	NIT-GC1 full	comp411593_c0_seq1_2717_R		GTGCTATCATTCCAG
Recombinant DNA reagent	NIT-GC2 full	Contig2280_66_F		AATATCTAGCGAAGGA
Recombinant DNA reagent	NIT-GC2 full	Contig2280_2763_R		ATGCCAGTAATAAAC
Recombinant DNA reagent	pcDNA3.1(+) vector	Invitrogen	Catalog Number: V79020	
Recombinant DNA reagent	Inverse PCR for the insert region of pcDNA3.1(+)	pcDNA3.1(+)_inv_NheI_fwd		CGTTTAAACTTAAGCT
Recombinant DNA reagent	Inverse PCR for the insert region of pcDNA3.1(+)	pcDNA3.1(+)_inv_NheI_rev		CCAGCTTGGGTCTCC
Recombinant DNA reagent	kozak-NITGC2-T2A-Green cGull	NITGC-T2A-fwd		TATAGGGAGACCCAA
Recombinant DNA reagent	kozak-NITGC2-T2A-Green cGull	NITGC-T2A-rev1		GCATGTTAGAAGACT
Recombinant DNA reagent	kozak-NITGC2-T2A-Green cGull	NITGC-T2A-rev2		AGGGCCGGGATTCTC
Recombinant DNA reagent	kozak-NITGC2-T2A-Green cGull	NITGC-T2A-rev3		TGCTCACCATAGGGC
Recombinant DNA reagent	kozak-NITGC2-T2A-Green cGull	cGull-fwd		TCCCGGCCCTATGGTC
Recombinant DNA reagent	kozak-NITGC2-T2A-Green cGull	cGull-rev		ACCAAGCTTAAGTTA
Recombinant DNA reagent	Green cGull-T2A-NITGC2 & NITGC2-T2A-Green cGull	NITGC2_seq_743_fwd		AGCCATCTACGAGTGC
Recombinant DNA reagent	Green cGull-T2A-NITGC2 & NITGC2-T2A-Green cGull	cGull_seq_385_rev		TGCCCTTCAGCTCGA
Recombinant DNA reagent	Green cGull-T2A-NITGC2 & NITGC2-T2A-Green cGull	NITGC2_seq_743_rev		TGACTGACGAACCCTC
Recombinant DNA reagent	Green cGull-T2A-NITGC2 & NITGC2-T2A-Green cGull	NITGC2_seq_394_fwd		AGATATCTTGAAACGC
Recombinant DNA reagent	kozak-NIT1(seq)-T2A-Green cGull	2A-cGull_invF_L1		TGACGTGGAGGAGAA
Recombinant DNA reagent	kozak-NIT1(seq)-T2A-Green cGull	2A-cGull_invF_L2		GCAGAGGAAGTCTTC

Reagent type (species)	Designation	Source or reference	Identifiers	Additional information
Recombinant DNA reagent	kozak-NIT1(seq)-T2A-Green cGull	2A-cGull_invR_L		TCCTTGCTTGTCACTGGC
Recombinant DNA reagent	kozak-NIT1(seq)-T2A-Green cGull	NIT1-2A_F_L		GAGACCCAAGCTGGG
Recombinant DNA reagent	kozak-NIT1(seq)-T2A-Green cGull	NIT1-2A_R_L		TGTTAGAACAGACTTCCT
Recombinant DNA reagent	kozak-NIT1(seq)-T2A-Green cGull	NIT1seq_remo_invF2		AGCGTGGAGGTGGGC
Recombinant DNA reagent	kozak-NIT1(seq)-T2A-Green cGull	NIT1seq_remo_invR2		AGCTCTTCGTCTAGC
Recombinant DNA reagent	kozak-NIT1(seq)-T2A-Green cGull	NIT1seq_remo_F2		GCCGGTCTTGTGATC
Recombinant DNA reagent	kozak-NIT1(seq)-T2A-Green cGull	NIT1seq_remo_R2		GTCCAGATCATCCTGA
Recombinant DNA reagent	pUC57-NOSp::Palmitoyl-3xHA-tdTomato (plasmid)	This paper		Promoter construct:
Recombinant DNA reagent	pUC57-T7-RPP2-tdTomato-P2A-GCaMP6 (plasmid)	This paper		Used for generating t
Plasmid	Green cGull	Addgene	Plasmid #86867	
HCR	NOS	Integrated DNA Technologies		
HCR	NIT-GC1	Integrated DNA Technologies		
HCR	NIT-GC2	Integrated DNA Technologies		
HCR	RYa-pNP (GenBank accession: JF811330.1)	Integrated DNA Technologies		
HCR	c-opsin1 (GenBank accession: AY692353.1)	Integrated DNA Technologies		
HCR	MLD/pedal2-pNP (GenBank accession: KF515945.1)	Integrated DNA Technologies		
HCR	CNGA $\alpha$ (GenBank accession: KM199644.1)	Integrated DNA Technologies		
fluorescently labeled hairpins	B2-647	Molecular Technologies		
fluorescently labeled hairpins	B3-546	Molecular Technologies		
morpholino	NIT-GC1 MO1	Gene-Tools, LLC		TGCTTGTCAATTATTCA
morpholino	NIT-GC1 MO2	Gene-Tools, LLC		TTCAATTAAACCCTCC
morpholino	NIT-GC2 MO1	Gene-Tools, LLC		AAATGAAGAGAGGTG
morpholino	NIT-GC2 MO2	Gene-Tools, LLC		ATATTCAATTATGTGAA
plasmid for mRNA synthase (GCaMP6s)	BamHI-T7::RPP2(5UTR)-GCaMP6s(Ascl-Agel)-polyA_KpnI_c1		Plasmid	Bezares-Calderón et
plasmid for mRNA synthase (RGECO1a)	PUC57-T7-PduRPP2(5UTR)-jRGECO1a		Plasmid	Bezares-Calderón et
Chemical compound, drug	SNAP	Sigma-Aldrich	Cat#:M9020	500 μM
Chemical compound, drug	L-NAME	Sigma-Aldrich	Cat#:M9021	500 μM

Reagent type (species)	Designation	Source or reference	Identifiers	Additional information
Chemical compound, drug	DMEM, low glucose	Thermofisher	Cat#:11885084	
Commercial assay or kit	Phusion Human Specimen Direct PCR Kit	Thermofisher		
Commercial assay or kit	mMESSAGE mMACHINE Sp6 kit	Thermofisher		
Software, algorithm	Golden Gate TAL	Addgene 1000000024 PMID: 22743772, <a href="https://github.com/JekelyLab/Veraszto_et_al_2018">https://github.com/JekelyLab/Veraszto_et_al_2018</a>		
Software, algorithm	Effector Kit 2.0, Fiji perl and Fiji scripts for tracking	<a href="https://github.com/JekelyLab/Veraszto_et_al_2018">https://github.com/JekelyLab/Veraszto_et_al_2018</a>	RRID:SCR_002285	0000d2a
Commercial assay or kit	QuickExtract	Epicentre,US	Cat#:QE09050	
Commercial assay or kit	MEGAshortscript T7 Transcription Kit	Ambion, ThermoFisher Scientific	Cat#:AM1354	
Commercial assay or kit	mMESSAGE mMACHINE T7Ambion, ThermoFisher ULTRA Transcription Kit	Ambion, ThermoFisher Scientific	Cat#:AM1345	
Commercial assay or kit	MEGAclear Transcription Clean-Up Kit	Ambion, ThermoFisher Scientific	Cat#:AM1908	
Software, algorithm	Fiji	NIH	RRID:SCR_002285	
Software, algorithm	R Project for Statistical Computing	R Foundation	RRID:SCR_001905	
Software, algorithm	Imaris Version 8.0.0	Bitplane, UK. <a href="https://doi.org/10.1101/bioinformatics/btp266">DOI:10.1101/bioinformatics/btp266</a>	RRID:SCR_007370	
Software, algorithm	CATMAID	<a href="https://doi.org/10.1101/bioinformatics/btp266">DOI:10.1101/bioinformatics/btp266</a>	RRID:SCR_006278	
Software, algorithm	IQ-tree2	DOI: 10.1101/molbev/msaa131RRID:SCR_017254		
Software, algorithm	TrimAL	DOI: 10.1101/bioinformatics/btp348	RRID:SCR_017334	
Software, algorithm	MAFFT	DOI: 10.1101/molbev/mst010	RRID:SCR_011811	
Software, algorithm	cd-hit	<a href="http://cd-hit.org/">http://cd-hit.org/</a>		
Software, algorithm	clans	DOI: 10.1101/bioinformatics/bth444		
Software, algorithm	Hmmer	<a href="http://hmmer.org/">http://hmmer.org/</a>	RRID:SCR_005305	

## Materials and Methods

### CRISPR-Cas9 design and Microinjection

For the generation of a *NOS* knockout, we used an sgRNA targeting the third exon of the *Platynereis dumerilii NOS* gene (target site: 5'-GGGCAATACTGGCTCCACTC-3'). We selected the site to avoid polymorphic sites in our laboratory culture. The sgRNA was assembled from two annealed oligonucleotides (5'-TAGGGCAATACTGGCTCCACTC-3', 5'-AACCGAGTGGAGGCCAGTATTGC-3') forming overhangs for cloning into the Bsal site of the plasmid pDR27456 @hwang2013 (42250,%20Addgene), which contains next to the Bsal site a tracrRNA sequence. We used this plasmid to PCR amplify DNA (primers: T7, 5'-AAAAGCACCGACTCGGTGCC-3') for synthesizing the sgRNA. To purify the PCR product, we used the QIAquick PCR Purification Kit (Qiagen). We then synthesized sgRNA with the MEGAshortscript Kit (Thermo Fisher Scientific) and purified it with the MEGAclear Kit (Thermo Fisher Scientific). To produce the Cas9-mRNA, we used the plasmid (pUC57-T7-

RPP2-Cas9) containing the Cas9 ORF fused to 169 base pair 5' UTR from the *Platynereis dumerilii* 60S acidic ribosomal protein P2. After in vitro transcription with the mMessage mMachine Kit (Thermo Fisher Scientific), we capped and polyA-tailed the Cas9-mRNA with the Poly(A) Tailing Kit (Thermo Fisher Scientific). We coinjected the sgRNA (18 ng/ml) and the Cas9-mRNA (180 ng/μl) into fertilized eggs of *Platynereis dumerilii* wild-type parents according to an established injection procedure (Conzelmann et al., 2013a). Eggs were kept at 18°C for 45 min before injection and were injected at 14.5°C. The injected individuals were kept at 18°C for 5 to 8 days in 6-well-plates (Nunc multidish no. 150239, Thermo Scientific) and then cultured at 22°C until sexual maturity. The mature worms were crossed to wild-type worms and the progeny was genotyped, resulting in two founder lines, which were bred to homozygosity.

### Genotyping of NOS alleles

For genotyping of the *NOS* locus, genomic DNA was isolated from single larvae, groups of 6-20 larvae, or from the tails of adult worms. The DNA was amplified by PCR (primers: 5'-GGTCATTGGTTCGATAACATTGCGG-3', 5'-CAGAGTCGATCAGTCTGCATATCTCA-3') with the dilution protocol of the Phusion Human Specimen Direct PCR Kit (Thermo Scientific). The PCR product was sequenced directly with a nested sequencing primer (5'-GGTGCTCTCCGGGTACACAA-3'). A mixture of wild-type and deletion alleles in a sample gave double peaks in the sequencing chromatograms, with the relative height of the double peaks reflecting the relative allele ratio in the sample.

### Morpholino-mediated knockdowns

Morpholino injections were performed as previously described (Conzelmann et al., 2013b). We used the following morpholinos to target the NIT-GC1 and NIT-GC2 genes (GeneTools, LLC). NIT-GC1 MO1: TGCTTGTCAATTATTCAACCAGCAAA, NIT-GC1 MO2: TTCAATTAAACCCCTCCAGGTTGCTG, NIT-GC2 MO1: AAATGAAGAGAGGTGTTCTCCTTCG, NIT-GC2 MO2: ATATTCATTATGTGAAGAACTTCCA.

### Vertical column setup to measure photoresponses

We assayed larval photoresponses in a vertical Plexiglas column (31 mm x 10 mm x 160 mm water height). For stimulation, we illuminated the column from above with a monochromator (Polychrome II, Till Photonics) controlled by AxioVision 4.8.2.0 (Carl Zeiss GmbH, Jena) via analog voltage. The light passed a collimator lens (LAG-65.0-53.0-C with MgF<sub>2</sub> Coating, CVI Melles Griot) before entering the column. The column was illuminated from both sides with light-emitting diodes (LEDs). The LEDs on each side were grouped into two strips. One strip contained UV (395 nm) LEDs (SMB1W-395, Roithner Lasertechnik) and the other infrared (810 nm) LEDs (SMB1W-810NR-I, Roithner Lasertechnik). The UV LEDs were run at 4 V. The infrared LEDs were run at 8 V (overvoltage) to illuminate the larvae for imaging with a DMK camera (DMK 22BUC03, The Imaging Source). We recorded videos at 15 frames per second with the software IC Capture (The Imaging Source).

We compared the behavior of wildtype and *NOS*-knockout larvae in the vertical column. In the inhibitor experiments we compared wildtype larvae before and after treatment with 0.1 mM or 1.0 mM NOS inhibitor L-NAME (in seawater). All larvae were three days oldt. Before the experiment, the larvae were mixed and left in the dark for 5 min. The larvae were recorded for 1.5 min in the dark followed by exposure to diffuse UV light (395 nm) from the side for 2 min. Then the larvae were left for another 2 min in darkness followed by exposue to collimated cyan (480 nm) light from above for 2 min, then 2 min darkness, and finally collimated UV (395 nm) light from above for 2 min. Scripts are available at [https://github.com/JekelyLab/Jokura\\_et\\_al\\_NOS](https://github.com/JekelyLab/Jokura_et_al_NOS) ([https://github.com/JekelyLab/Jokura\\_et\\_al\\_NOS](https://github.com/JekelyLab/Jokura_et_al_NOS)).

### Identification and Phylogenetic Analysis of NOS sequences

To identify NOS sequences, we obtained a seed database of oxygenase domains from the Pfam database (PF02898). From these sequences, we generated a Hidden Markov Model (HMM) to mine the genomes and transcriptomes of 47 metazoan, 2 choanoflagellate and 2 filasterea species. The HMM model was run in HMMR3 (Eddy, 2011) with an e-value of 1e-15. We ran CD-Hit (Fu et al., 2012) to eliminate redundant sequences (at a 80% threshold). We aligned the sequences with MAFFT version 7, with the iterative refinement method E-INS-i (Katoh and Toh, 2008). The alignment was trimmed with TrimAl in gappy-out mode (Capella-Gutierrez et al., 2009). To calculate a maximum-likelihood tree, we used IQ-tree2 with the LG+G4 model with the following options: iqtree2 -s "FILENAME" -mset WAG, LG, Blosum62, Dayhoff, JTT, Poisson -B 1000 -alrt 1000 -T AUTO. Branch-support values are based on 1000 replicates with the ultrafast bootstrap approximation (UFBoot) (Hoang et al., 2018) and aLRT-SH-like (Guindon et al., 2010) methods.

### Identification and Phylogenetic Analysis of NIT-GC sequences

To identify NIT-GCs, we obtained a seed database of adenylate and guanylate cyclase catalytic domains from the Pfam database (PF00211). From these sequences, we generated a Hidden Markov Model (HMM) to mine the 45 metazoan, 2 choanoflagellate and 2 filasterea genomes and transcriptomes. The HMM model was run in HMMR3 (Eddy, 2011) with an e-value of 1e-15. We ran CD-Hit (Fu et al., 2012) to eliminate redundant sequences (at a 80% threshold). To identify clusters, we used sequence-similarity-based clustering in Clans (Frickey and Lupas, 2004) and the convex-clustering option with 100 jack-knife replicates. The NIT-GCs are extremely well conserved within the membrane-bound guanylate cyclases and form an easily recognizable cluster. To analyze the phylogeny of NIT-GCs, the cluster containing these GCs together with membrane-bound guanylate cyclases were parsed and used for tree building. We aligned the sequences with MAFFT version 7, with the iterative refinement method E-INS-i (Katoh and Toh, 2008). The alignment was trimmed with TrimAl in gappy-out mode (Capella-Gutierrez et al., 2009). To calculate a maximum-likelihood tree, we used IQ-tree2 with the LG+G4 model with the following options: iqtree2 -s "FILENAME" -mset WAG, LG, Blosum62, Dayhoff, JTT, Poisson -B 1000 -alrt 1000 -T AUTO. Branch-support values are based on 1000 replicates with the ultrafast bootstrap approximation (UFBoot) (Hoang et al., 2018) and aLRT-SH-like (Guindon et al., 2010) methods.

### Single-cell analysis

We used a single-cell RNA sequencing dataset from *Platynereis* larvae (Achim et al., 2015) that was further filtered to 107 cells (Williams et al., 2017). We normalized the raw read-count data to TPM and converted to log10. To calculate % expression, we used the sum of the expression levels in the 107 cells for each gene. The total TPM of each gene between the samples was used to calculate the percentage of expressed genes. We processed the data in Python and plotted in R. Individual cells were identified by suits of well-characterised marker genes and spatial mapping (Achim et al., 2015).

### In situ HCR

Larvae were fixed and treated with Proteinase K, according to the conventional WMISH protocol (Tessmar-Raible et al., 2005), with fixation in 4% paraformaldehyde/ PTW (PBS with 0.05% Tween20) for 2 hr at room temperature, and Proteinase K treatment in 100 µg/ml Proteinase K/ PTW for 3 min (Tessmar-Raible et al., 2005). Specifically, for the HCR protocol, samples were processed in 1.5 ml tubes. Probe hybridization buffer, probe wash buffer, amplification buffer, and fluorescent HCR hairpins were purchased from Molecular Instruments (Los Angeles, USA). The hairpins associated with the b2 initiator sequence were labeled with Alexa Fluor 647, and the hairpins associated with the b3 initiator sequence were labeled with Alexa Fluor 546. To design probes for HCR, we used custom software (Kuehn et al., 2021) to create 20 DNA oligo probe pairs specific to *P. dumerilii* NOS, NIT-GC1, NIT-GC2, *RYa proneuropeptide* (GenBank accession: JF811330.1), and *MLD/pedal peptide 2 proneuropeptide* (GenBank accession: KF515945.1). The NOS, NIT-GC1 and NIT-GC2 probes were designed to be associated with the b2 initiator sequence, while the *RYa* and *MLD/pedal peptide 2* probes were designed to be associated with the b3 initiator sequence. For the detection stage, samples were pre-hybridized in 200 µl of probe hybridization buffer for 1 hr at 37°C, and then incubated in 250 µl hybridization buffer containing probe oligos (4 pmol/ml) overnight at 37°C. To remove excess probe, samples were washed 4x with 1 ml hybridization wash buffer for 15 min at 37°C, and subsequently 2x in 1 ml 5× SSCT (5× SSC with 0.1% Tween20) for 5 min at room temperature. For the amplification stage, samples were pre-incubated with 100 µl of amplification buffer for 30 min, room temperature, and then incubated with 150 µl amplification buffer containing fluorescently labelled hairpins (40nM concentration (2ul of 3uM stock in 150ul amplification buffer, snap-cooled as described; (Choi et al., 2018)) overnight in the dark at 25°C. To remove excess hairpins, samples were washed in 1 ml 5× SSCT at room temperature, twice for 5 min, twice for 30 min, and once for 5 min. During the first 30 min wash, samples were counterstained with DAPI (Cat. #40043, Biotium, USA).

### Immunohistochemistry

Whole-mount immunostaining of *Platynereis* larvae fixed with 4% paraformaldehyde was carried out using the primary antibodies listed in the KEY RESOURCES TABLE. Immunostainings were carried out as previously described (Conzelmann and Jékely, 2012).

### Antibody generation and purification

Antibodies were raised in rats or rabbits against synthetic peptides containing an N-term Cys residue (Altabioscience). The same Cys-containing synthetic peptides were used for affinity purification. Antibodies were affinity purified from sera on a SulfoLink Coupling Resin (Thermo Fischer) as previously described (Conzelmann and Jékely, 2012). View a detailed protocol here: <https://bio-protocol.org/exchange/preprintdetail?id=2333&type=3> (<https://bio-protocol.org/exchange>)

## Transient transgenesis

A 12 kb genomic region upstream of the start site of the *NOS* gene was amplified and cloned upstream of 3xHA-Palmi-*tdTomato* to yield the plasmid *NOS-3xHA-Palmi-tdTomato*. Larvae injected with the promoter construct (ca. 250 ng/ml) were analysed for reporter expression at three days post fertilization on an AxioImager Z.1 fluorescence microscope (Carl Zeiss GmbH, Jena) and if positive were fixed for immunostaining. The immunostaining for the HA-tagged reporter was done as described (Verasztó et al., 2017). Stained specimens were imaged on an LSM 780 NLO or LSM 880 Airysan Confocal Microscope (Carl Zeiss GmbH, Jena).

## Calcium imaging

For  $\text{Ca}^{2+}$  imaging, GCaMP6s mRNA (1 mg/ml) was injected into zygotes as described previously (Randel et al., 2014). At 49-55 hours post fertilisation, larvae were immobilised in 2.5% agarose in artificial sea water and mounted between a slide and coverslip spaced with adhesive tape. Larvae were imaged at room temperature on a Zeiss LSM 880 with Airyscan (with a C-Apochromat 63X/1.2 Corr - water) with a frame rate of 1.88 frame/sec and an image size of 512 x 512 pixels. The larvae were stimulated in a region of interest (a circle with 50 pixel diameter) with a 405 nm laser controlled by the bleaching mode of the Zeiss software. The imaging laser had a similar intensity than the stimulus laser but covered an area that was 10 times larger than the stimulus ROI.

## cGMP production assay

To measure cGMP production in a cell culture assay we used the Green cGull reporter (Matsuda et al., 2016). Full-length *NIT-GC1* and *NIT-GC2* coding sequences were amplified by PCR from a *Platynereis dumerilii* cDNA library and cloned into the pcDNA3.1(+) vector with the T2A self-cleaving sequence. For the assay, COS-7 cells (Angio-proteomie, CAT no. cAP-0203) with a low endogenous level of soluble guanylate cyclase activity were used. Cells were not contaminated with mycoplasma. Cells were maintained at 37 °C in 35 mm dishes (Nunc™ Glass Bottom Dishes) containing 3 ml of DMEM, low-glucose medium (Thermo; Cat. No. 11885084) supplemented with 10% fetal bovine serum (Thermo; Cat. No. 10082147). Upon reaching approximately 85% confluence, cells were transfected with the pcDNA3.1(+)–Green-cGull-T2A-NITGC1 plasmid. Transfections were carried out with 150 ng of each plasmid and 0.3 µl of Lipofectamine 3000 Reagent (Invitrogen; Cat. No. L3000001). Three hours post-transfection, the culture medium was substituted with fresh DMEM medium. For single-wavelength imaging experiments, cells in 35-mm dishes were washed twice and imaged in modified Ringer's buffer (140 mM NaCl, 3.5 mM KCl, 0.5 mM  $\text{NaH}_2\text{PO}_4$ , 0.5 mM S-3 MgSO<sub>4</sub>, 1.5 mM CaCl<sub>2</sub>, 10 mM HEPES, 2 mM NaHCO<sub>3</sub> and 5 mM glucose). The dishes were mounted on a stage heated to 37 °C and imaged on an inverted confocal microscope (LSM880, Carl Zeiss GmbH, Jena) equipped with an oil-immersion objective lens (UApO/340, 40x, NA = 0.17). The exposure time of the EM-CCD camera was controlled by the ZEN software (Carl Zeiss GmbH, Jena). Images were acquired every 15 s for 10 min and stimulation was initiated 2 min after starting image acquisition. Imaging data were processed with ImageJ (National Institutes of Health, Bethesda, MD, USA). As NO donor, we used S-Nitroso-N-acetyl-D, L-penicillamine (SNAP, Sigma-Aldrich, St.

# Mathematical modelling

## Wild type model

The mathematical model for the wild type data comprises six dynamical equations:

$$\begin{aligned}
\frac{dC_P(t)}{dt} &= 1 - \delta^{C_P} C_P(t) + K_{UV}^{C_P} UV(t) C_O(t) + K_G^{C_P} G(t), \\
\frac{dC_O(t)}{dt} &= 1 - \delta^{C_O} C_O(t) - K_{UV}^{C_O} UV(t) C_O(t), \\
\frac{dG(t)}{dt} &= 1 - \delta^G G(t) + K_{GC2}^G (1 - UV(t)) G(t) + K_{GC1}^G N(t), \\
\frac{dS(t)}{dt} &= UV(t) - \frac{S(t)}{\tau_S}, \\
\frac{dC_N(t)}{dt} &= 1 - \delta^{C_N} C_N(t) + K_S^{C_N} S(t), \\
\frac{dN(t)}{dt} &= 1 - \delta^N N(t) + K_{C_N}^N C_N(t), \\
\frac{dC_R(t)}{dt} &= 1 - \delta^{C_R} C_R(t) - K_S^{C_R} S(t) + K_{C_P}^{C_R} C_P(t) - K_{C_N}^{C_R} C_N(t) C_R(t), \\
UV(t) &= \begin{cases} a, & t_{UV \ start} \leq t \leq t_{UV \ end} \\ 0, & \text{otherwise} \end{cases}.
\end{aligned}$$

The  $C_P(t)$  equation describes the dynamics of the  $\text{Ca}^{2+}$  concentration in the cPRC cells. The  $K_{UV}^{C_P} UV(t) C_O(t)$  term captures the  $\text{Ca}^{2+}$  increase due to c-opsin1 activity induced by UV stimulation, while the  $K_G^{C_P} G(t)$  term captures dependence of the  $\text{Ca}^{2+}$  dynamics on cGMP. The  $C_O(t)$  equation is added to capture the decrease of the  $\text{Ca}^{2+}$  levels observed during the UV stimulation; the mechanism of this decrease is unknown. It could, for example, be related to the opening of the GIRK channels. The  $G(t)$  equation describes the dynamics of cGMP in the cPRC cells. The  $K_{GC1}^G N(t)$  term describes the NO-dependent increase in cGMP by NIT-GC1, while the  $K_{GC2}^G (1 - UV(t)) G(t)$  term captures the cGMP decrease mediated by NIT-GC2 during UV stimulation. The  $S(t)$  describes synaptic coupling from the cPRC cells, which is assumed to act in an excitatory fashion on INNOS cells and an inhibitory fashion on INRGW cells. This coupling is assumed to be suppressed in NIT-GC2 morphants. The  $C_N(t)$  equation describes the  $\text{Ca}^{2+}$  dynamics in the INNOS cells. The  $K_S^{C_N} S(t)$  term describes the  $\text{Ca}^{2+}$  increase due to the synaptic signal  $S(t)$ . The  $N(t)$  variable represents NO produced and secreted by the INNOS cells. The  $K_{C_N}^N C_N(t)$  term describes the  $\text{Ca}^{2+}$ -dependent NO production within the INNOS cells. The  $C_R(t)$  equation describes the dynamics of  $\text{Ca}^{2+}$  in the INRGW cells, which depends on the other equations in a feed-forward manner. The  $K_S^{C_R} S(t)$  and  $K_{C_N}^{C_R} C_N(t) C_R(t)$  terms describe the decrease in  $\text{Ca}^{2+}$  with respect to the synaptic signal  $S(t)$  and the  $\text{Ca}^{2+}$  levels in the INNOS cells, respectively. The  $K_{C_P}^{C_R} C_P(t)$  term describes the increase in  $\text{Ca}^{2+}$  levels in the INRGW cells due to increases in the  $\text{Ca}^{2+}$  levels in the cPRC cells. Note that all sources of  $\text{Ca}^{2+}$  variation in the INRGW cells are phenomenological in nature. All variables have a constant (unit) production term and a linear decay rate set by the parameter  $\delta_X$  where  $X \in \{C_P, C_O, G, S, C_N, C_R\}$ . Finally, the UV stimulation is described by a square pulse with amplitude  $a$  and duration  $t_{UV \ end} - t_{UV \ start}$ .

## NOS-knockout model

The NOS-knockout model is derived from the WT model by eliminating the  $N(t)$  variable, which represents the NO produced by the INNOS cells in a NOS-dependent manner, and terms that depend on it. This gives the system

$$\begin{aligned}
\frac{C_P(t)}{dt} &= 1 - \delta^{C_P} C_P(t) + K_{UV}^{C_P} UV(t) C_O(t) + K_G^{C_P} G(t), \\
\frac{C_O(t)}{dt} &= 1 - \delta^{C_O} C_O(t) - K_{UV}^{C_O} UV(t) C_O(t), \\
\frac{G(t)}{dt} &= 1 - \delta^G G(t) + (1 - UV(t)) K_{GC_2}^G G(t), \\
\frac{S(t)}{dt} &= UV(t) - \frac{S(t)}{\tau_S}, \\
\frac{C_N(t)}{dt} &= 1 - \delta^{C_N} C_N(t) + K_S^{C_N} S(t), \\
\frac{C_R(t)}{dt} &= 1 - \delta^{C_R} C_R(t) - K_S^{C_R} S(t) + K_{C_P}^{C_R} C_P(t) - K_{C_N}^{C_R} C_N(t) C_R(t), \\
UV(t) &= \begin{cases} a, & t_{UV \ start} \leq t \leq t_{UV \ end} \\ 0, & \text{otherwise} \end{cases}.
\end{aligned}$$

We remark that the above system of equations can be used to also describe the NIT-GC1 morpholino condition (Fig. 4M).

## NIT-GC2 morpholino model

The NIT-GC2 morpholino model is a further restriction of the WT model:

$$\begin{aligned}
\frac{C_P(t)}{dt} &= 1 - \delta^{C_P} C_P(t) + K_{UV}^{C_P} UV(t) C_O(t), \\
\frac{C_O(t)}{dt} &= 1 - \delta^{C_O} C_O(t) - K_{UV}^{C_O} UV(t) C_O(t), \\
\frac{C_R(t)}{dt} &= 1 - \delta^{C_R} C_R(t) + K_{C_P}^{C_R} C_P(t), \\
UV(t) &= \begin{cases} a, & t_{UV \ start} \leq t \leq t_{UV \ end} \\ 0, & \text{otherwise} \end{cases}.
\end{aligned}$$

This reduced model eliminates the  $G(t)$ ,  $S(t)$ ,  $C_N(t)$  and  $N(t)$  variables and hence includes only c-opsin1 activity in the cPRC cells and the feedforward coupling to INRGW cells. The synaptic signal  $S(t)$  and all terms depending on it are removed due to the assumed dependence on NIT-GC2. When the  $S(t)$  input is disregarded, the activity of the INNOS cells ( $C_N(t)$  and  $N(t)$  variables) can be represented by a constant steady state whose values can subsequently be absorbed into all the terms depending on these variables. Hence these variables are eliminated in the reduced model. Since the  $K_{GC_2}^G (1 - UV(t)) G(t)$  term depends directly on NIT-GC2 and when  $N(t)$  is ignored the  $K_{GC_1}^G N(t)$  term disappears, the  $G(t)$  variable can be eliminated, which consequently simplifies the  $C_P(t)$  equation. The only remaining term in  $C_R(t)$  equation,  $K_{C_P}^{C_R} C_P(t)$ , describes feedforward coupling between the cPRC and INRGW cells.

## Parameter fitting (genetic algorithm)

To find sets of model parameters that reproduce recordings from the  $\text{Ca}^{2+}$  imaging experiments, we define an optimisation problem to minimise the discrepancy between the modelled  $\text{Ca}^{2+}$  traces and the experimental data. To obtain the modelled  $\text{Ca}^{2+}$  traces, we run the model using the Matlab built-in solvers to find the steady state in the absence of UV stimulation, and then use the explicit integration algorithm to simulate the model with the computed steady state as the initial condition.

We quantify the difference between the model output and the data using a vector-valued objective function. The first component of this function measures this difference during the UV stimulation, whilst the second component measures the difference from the end of the stimulation until the end of the recording. We thus define a vector-valued objective function,  $\mathbf{D} \in \mathbb{R}_{\geq 0}^2$ , as:

$$\mathbf{D} \left( C_X^{data}, C_X^{model} \right) = \left( D_{k_{UV \ start}}^{k_{UV \ end}} \left( C_X^{data}, C_X^{model} \right), D_{k_{UV \ end}+1}^{k_{end}} \left( C_X^{data}, C_X^{model} \right) \right),$$

with

$$D_{k_1}^{k_2} \left( C_X^{data}(t), C_X^{model}(t) \right) = \sqrt{\sum_{i=k_1}^{k_2} \left( C_X^{data}(t_i) - C_X^{model}(t_i) \right)^2},$$

where the timepoints  $t_i = i\Delta t$  are equispaced with  $\Delta = 0.5s$  and where  $t_{k_{UV start}} = t_{UV start}$  (and similar for the other time points). Here  $C_X^{data}$  denotes normalised experimental data and  $C_X^{model}$  denotes normalised simulated  $\text{Ca}^{2+}$  trace with  $X \in \{P, N, R\}$  indicating cell type. Simulated  $\text{Ca}^{2+}$  traces,  $C_X^{model}$ , are normalised in the same way as the experimental data, i.e., we divide values uniformly by their value at  $t_{k_{UV start}-1}$ , a time point immediately prior to the start of the UV stimulation. Simulations are sampled with the same sampling rate as the data. (Recall that  $t_{UV start}$  is the time of the start of UV stimulation,  $t_{UV end}$  is the time of the end of UV stimulation, and  $t_{end}$  is the last time sample.)

To solve the optimisation problem with the above objective function, we employ a global optimisation method known as a genetic algorithm (GA). GAs are a class of iterative, gradient-free algorithms inspired by processes of natural selection including breeding and mutation. In reference to natural selection, sets of candidate solutions in GAs are referred to as ‘populations’. As our algorithm of choice, we use the Matlab implementation of a genetic algorithm for multiobjective optimisation. The algorithm uses a controlled, elitist genetic algorithm (a variant of NSGA-II). We use the default settings for most hyperparameters of the algorithm.

Here we outline the main steps of the implementation of the GA. The first step is to generate a set of random model parameter sets, known as the initial population. Next, we score the fitness of each parameter set in the population according to the objective function. Using these scores, the algorithm employs a binary tournament selection function to select ‘parents’ for the next population. A population of children (i.e., new parameter sets) is generated by ‘breeding’ randomly chosen pairs of parents (exchanging subsets of parameter values between them). Parameter values in these children can also be changed by ‘mutations’, which perturb said values randomly by a small amount. Breeding and mutation introduce a level of randomness to the optimisation process that allows exploring the objective function (fitting) landscape. The stochastic nature of GAs helps them to avoid local minima that can plague gradient-descent-based optimisation methods.

In the next step, the algorithm scores the parameter sets in the children population using the values of the objective function. Scores from the parent and child populations are combined. A subset of the size of the initial population is then selected as a new parent population based on the scores and the distance to other parameter sets in terms of a sum of element-wise differences between values of the objective function (used to ensure diversity of the parent population). This iterative process is repeated until the convergence criteria are met, indicating that the GA has found a set of model parameters that best reproduce the data under consideration.

The algorithm returns a set of model parameter values on a Pareto front. The coordinates of points on the front are the values of the components of the objective function  $\mathbf{D}$ . Points on the Pareto front are nondominated, meaning that they are closest to 0 for at least one of the two components. To identify a single optimal solution, we select the parameter set along the Pareto front whose objective function value is the smallest with respect to the Euclidean norm.

Below we present a summary of the steps of our optimisation pipeline for fitting the experimental recordings from the cPRC cells.

- When fitting to the cPRC data using WT or NIT-GC2 morpholino models, we eliminate the  $C_R(t)$  variable since it does not have any feedback coupling with the  $C_P(t)$  equation and does not affect its dynamics. When fitting to the cPRC data using the NOS-knockout model, we also eliminate the  $S(t)$ ,  $C_N(t)$  and  $C_R(t)$  variables since these do not have any effect on the  $C_P(t)$ .
- Set the size of the initial population to 1,000. This value provides a compromise in terms of the coverage of the parameter space and run-time of the GA.
- Set bounds of random distributions of parameters. We draw all the initial parameter values from uniform distributions over the unit interval ([0,1]). For WT condition, we fit 13 parameters, for NOS-knockout, we fit 7 parameters and for NIT-GC2 morpholino, we fit 4 parameters.
- Evaluate the objective function on the initial population.
- Run the algorithm.

- Repeat steps 1 to 4 with bounds of parameters extended to [0,5] and using the Pareto front returned in step 4 as a part of the initial population. This step was added after observing that, although good fits to most datasets are achieved with parameter values in the interval [0,1], fits to some datasets can be improved by extending the admissible parameter range.
- Use the Euclidean norm to find the set of model parameters that best fits the data.

Since INNOS cells in the NOS-knockout condition and INRGW cells in all conditions are coupled in a feedforward manner and do not affect the ‘up-stream’ dynamics, we run a separate optimisation to fit data from these cells. This minimises the number of parameters that are being fitted simultaneously and ensures that the objective function is as simple as possible (using only recordings from a cell type that is being fitted). First, we fix the parameters that were found by fitting the model to the cPRC data. Next, we run the optimisation in the same way as in the case of the cPRC data but only for the parameters that pertain to dynamics that is strictly ‘downstream’ of cPRC dynamics.

Fixing a subset of parameters allows us to ensure that model parameters inferred from recordings of one cell type stay relevant when fitting the model to the data from other cells. This means that the fitted model is extended to include other cell types, rather than being completely reparametrised for each cell type. This is particularly important since, for technical reasons, we do not have simultaneous recordings from multiple cell types.

We note that in the WT condition, model parameters of the INNOS cells are fitted without using any INNOS recordings. Since the NO production feeds back to the cPRC cells, their parameters are fitted to reproduce the recordings from the cPRC cells. Furthermore, in the NIT-GC2 morpholino condition, we do not fit the INNOS data since we assumed that the feedforward coupling between the cPRC cells and INNOS cell depends on NIT-GC2 activity (that is, we assume that the  $\text{Ca}^{2+}$  levels in INNOS cells are constant in this condition).

All the simulated curves presented in Fig. 6B are the averages of the curves fitted to individual experimental recordings/datasets.

## Predictions from a range of stimulation protocols

To explore possible effects of varying the intensity and duration of the UV stimulation on experimentally observed delayed activation in the cPRC cells, we perform a series of simulations in which we systematically varied amplitude ( $a \in [0.1, 1]$ ) and width ( $t_{UV\ end} \in [0.1, 51]$ ) of the  $UV(t)$  variable in the WT model. To quantify the effects of the stimulation, we measure the area under the peak of the delayed activation  $AUP$  in the  $C_P(t)$  variable. To compute the  $AUP$ :

- We find an inflection point that occurs after the start ( $t_{UV\ start}$ ) of the UV stimulation. To this end, we identify the first time point  $t_{AUP\ start} > t_{UV\ start}$  for which  $d^2C_P(t)/dt^2 = 0$  and  $d^2C_P(t_{k_{AUP\ start}} - 1)/dt^2 < d^2C_P(t_{k_{AUP\ start}})/dt^2 < d^2C_P(t_{k_{AUP\ start}} + 1)/dt^2$ . We assume that the inflection is caused by the input from the INNOS cells.
- We then compute the  $AUP$  as an integral over  $C_P(t)$  starting at the inflection point and ending 125 seconds later:  $\$AUP=*\{t*\{start\}\}^{\{t\_end\}} C_P(t) dt \$$ . To compute this, we use numerical integration via the trapezoidal method as implemented in Matlab function . We remark that the baseline value of the  $AUP$  for a  $\text{Ca}^{2+}$  profile of constant, unit value is 125.
- To capture possible variability between different cells/organisms, we compute the  $AUP$  using 47 model parameter sets fitted to individual WT cPRC experimental recordings. We remove outliers, defined as being any simulated traces for which  $C_P(t)$ , after normalisation, exits the interval [0.25, 4] at any time. This  $C_P(t)$  range was decided on the basis of values observed in various experiments in the lab.
- For analysis, we use the median value of the  $AUP$  at each combination of amplitude and duration.

Figure 7 shows how the results of the simulations of the WT model depend on the amplitude and duration of UV stimulation, as captured by the median values of  $AUP$ . Delayed activation occurs only for UV stimulation of sufficient amplitude and duration. Specifically, we observe sudden increase in  $AUP$  for UV pulse amplitude  $a > 0.5$  and a linear dependence of  $AUP$  on the pulse duration.

## Data analysis and figure preparation

Data were analysed in ImageJ and R. All figures were assembled in R with the cowplot and patchwork packages. All scripts are available at [https://github.com/JekelyLab/Joukra\\_et\\_al\\_NOS](https://github.com/JekelyLab/Joukra_et_al_NOS) ([https://github.com/JekelyLab/Joukra\\_et\\_al\\_NOS](https://github.com/JekelyLab/Joukra_et_al_NOS)) (commit: c223fe3).

## Acknowledgements

This work was funded by the Wellcome Trust (214337/Z/18/Z). This project has received funding from the European Research Council (ERC) under the European Union's Horizon 2020 research and innovation programme (grant agreement No 101020792). KJ has been supported by a JSPS Overseas Research Fellowship, LAYG by a BBSRC Discovery fellowship (BB/W010305/1), PS by a Wellcome Trust Institutional Strategic Support Award (204909/Z/16/Z), and KCAW by the EPSRC Hub for Quantitive Modelling in Healthcare (EP/T017856/1). We thank Dr. Francesca Carlisle for the mycoplasma testing of COS-7 cells.

## References

- Achim K, Pettit J-B, Saraiva LR, Gavriouchkina D, Larsson T, Arendt D, Marioni JC. 2015. High-throughput spatial mapping of single-cell RNA-seq data to tissue of origin. *Nature Biotechnology* **33**:503–509. doi:10.1038/nbt.3209 (<https://doi.org/10.1038/nbt.3209>)
- Arendt D, Tessmar-Raible K, Snyman H, Dorresteijn AW, Wittbrodt J. 2004. Ciliary Photoreceptors with a Vertebrate-Type Opsin in an Invertebrate Brain. *Science* **306**:869–871. doi:10.1126/science.1099955 (<https://doi.org/10.1126/science.1099955>)
- Aso Y, Ray RP, Long X, Bushey D, Cichewicz K, Ngo T-T, Sharp B, Christoforou C, Hu A, Lemire AL, Tillberg P, Hirsh J, Litwin-Kumar A, Rubin GM. 2019. Nitric oxide acts as a cotransmitter in a subset of dopaminergic neurons to diversify memory dynamics. *eLife* **8**. doi:10.7554/elife.49257 (<https://doi.org/10.7554/elife.49257>)
- Bargmann CI, Marder E. 2013. From the connectome to brain function. *Nature Methods* **10**:483–490. doi:10.1038/nmeth.2451 (<https://doi.org/10.1038/nmeth.2451>)
- Bezares-Calderón LA, Berger J, Jékely G. 2019. Diversity of cilia-based mechanosensory systems and their functions in marine animal behaviour. *Philosophical Transactions of the Royal Society B: Biological Sciences* **375**:20190376. doi:10.1098/rstb.2019.0376 (<https://doi.org/10.1098/rstb.2019.0376>)
- Bezares-Calderón LA, Shahidi R, Jékely G. 2023. A ciliary photoreceptor-cell circuit mediates pressure response in marine zooplankton (<http://dx.doi.org/10.1101/2023.02.28.530398>).
- Bishop CD, Brandhorst BP. 2007. Development of nitric oxide synthase-defined neurons in the sea urchin larval ciliary band and evidence for a chemosensory function during metamorphosis. *Developmental Dynamics* **236**:1535–1546. doi:10.1002/dvdy.21161 (<https://doi.org/10.1002/dvdy.21161>)
- Bray SR, Wyss LS, Chai C, Lozada ME, Wang B. 2023. Adaptive robustness through incoherent signaling mechanisms in a regenerative brain (<http://dx.doi.org/10.1101/2023.01.20.523817>).
- Bredt DS, Hwang PM, Snyder SH. 1990. Localization of nitric oxide synthase indicating a neural role for nitric oxide. *Nature* **347**:768–770. doi:10.1038/347768a0 (<https://doi.org/10.1038/347768a0>)
- Burette A, Zabel U, Weinberg RJ, Schmidt HHHW, Valtschanoff JG. 2002. Synaptic Localization of Nitric Oxide Synthase and Soluble Guanylyl Cyclase in the Hippocampus. *The Journal of Neuroscience* **22**:8961–8970. doi:10.1523/jneurosci.22-20-08961.2002 (<https://doi.org/10.1523/jneurosci.22-20-08961.2002>)
- Camargo A, Llamas A, Schnell RA, Higuera JoseJ, González-Ballester D, Lefebvre PA, Fernández E, Galván A. 2007. Nitrate Signaling by the Regulatory Gene *NIT2* in *Chlamydomonas*. *The Plant Cell* **19**:3491–3503. doi:10.1105/tpc.106.045922 (<https://doi.org/10.1105/tpc.106.045922>)
- Capella-Gutierrez S, Silla-Martinez JM, Gabaldon T. 2009. trimAl: a tool for automated alignment trimming in large-scale phylogenetic analyses. *Bioinformatics* **25**:1972–1973. doi:10.1093/bioinformatics/btp348 (<https://doi.org/10.1093/bioinformatics/btp348>)
- Choi HMT, Schwarzkopf M, Fornace ME, Acharya A, Artavanis G, Stegmaier J, Cunha A, Pierce NA. 2018. Third-generation *in situ* hybridization chain reaction: multiplexed, quantitative, sensitive, versatile, robust. *Development* **145**. doi:10.1242/dev.165753 (<https://doi.org/10.1242/dev.165753>)
- Conzelmann M, Jékely G. 2012. Antibodies against conserved amidated neuropeptide epitopes enrich the comparative neurobiology toolbox. *EvoDevo* **3**:23. doi:10.1186/2041-9139-3-23 (<https://doi.org/10.1186/2041-9139-3-23>)

- Conzelmann M, Offenburger S-L, Asadulina A, Keller T, Münch TA, Jékely G. 2011. Neuropeptides regulate swimming depth of *Platynereis* larvae. *Proceedings of the National Academy of Sciences* **108**. doi:10.1073/pnas.1109085108 (<https://doi.org/10.1073/pnas.1109085108>)
- Conzelmann M, Williams Elizabeth A, Krug K, Franz-Wachtel M, Macek B, Jékely G. 2013a. The neuropeptide complement of the marine annelid *Platynereis dumerilii*. *BMC Genomics* **14**:906. doi:10.1186/1471-2164-14-906 (<https://doi.org/10.1186/1471-2164-14-906>)
- Conzelmann M, Williams Elizabeth A, Tunaru S, Randel N, Shahidi R, Asadulina A, Berger J, Offermanns S, Jékely G. 2013b. Conserved MIP receptorligand pair regulates *Platynereis* larval settlement. *Proceedings of the National Academy of Sciences* **110**:8224–8229. doi:10.1073/pnas.1220285110 (<https://doi.org/10.1073/pnas.1220285110>)
- Cudeiro J, Rivadulla C. 1999. Sight and insight on the physiological role of nitric oxide in the visual system. *Trends in Neurosciences* **22**:109–116. doi:10.1016/s0166-2236(98)01299-5 ([https://doi.org/10.1016/s0166-2236\(98\)01299-5](https://doi.org/10.1016/s0166-2236(98)01299-5))
- Eddy SR. 2011. Accelerated Profile HMM Searches. *PLOS Computational Biology* **7**:1–16. doi:10.1371/journal.pcbi.1002195 (<https://doi.org/10.1371/journal.pcbi.1002195>)
- Frickey T, Lupas A. 2004. CLANS: a Java application for visualizing protein families based on pairwise similarity. *Bioinformatics* **20**:3702–3704. doi:10.1093/bioinformatics/bth444 (<https://doi.org/10.1093/bioinformatics/bth444>)
- Fu L, Niu B, Zhu Z, Wu S, Li W. 2012. CD-HIT: accelerated for clustering the next-generation sequencing data. *Bioinformatics* **28**:3150–3152. doi:10.1093/bioinformatics/bts565 (<https://doi.org/10.1093/bioinformatics/bts565>)
- Garthwaite J. 2015. From synaptically localized to volume transmission by nitric oxide. *The Journal of Physiology* **594**:9–18. doi:10.1113/jp270297 (<https://doi.org/10.1113/jp270297>)
- Gibbs SM, Truman JW. 1998. Nitric Oxide and Cyclic GMP Regulate Retinal Patterning in the Optic Lobe of Drosophila. *Neuron* **20**:83–93. doi:10.1016/s0896-6273(00)80436-5 ([https://doi.org/10.1016/s0896-6273\(00\)80436-5](https://doi.org/10.1016/s0896-6273(00)80436-5))
- Gühmann M, Jia H, Randel N, Verasztó C, Bezires-Calderón Luis A, Michiels Nico K, Yokoyama S, Jékely G. 2015. Spectral Tuning of Phototaxis by a Go-Opsin in the Rhabdomeric Eyes of *Platynereis*. *Current Biology* **25**:2265–2271. doi:10.1016/j.cub.2015.07.017 (<https://doi.org/10.1016/j.cub.2015.07.017>)
- Guindon S, Dufayard J-F, Lefort V, Anisimova M, Hordijk W, Gascuel O. 2010. New Algorithms and Methods to Estimate Maximum-Likelihood Phylogenies: Assessing the Performance of PhyML 3.0. *Systematic Biology* **59**:307–321. doi:10.1093/sysbio/syq010 (<https://doi.org/10.1093/sysbio/syq010>)
- Hoang DT, Chernomor O, Haeseler A von, Minh BQ, Vinh LS. 2018. UFBoot2: Improving the Ultrafast Bootstrap Approximation. *Molecular Biology and Evolution* **35**:518–522. doi:10.1093/molbev/msx281 (<https://doi.org/10.1093/molbev/msx281>)
- Hölscher C. 1997. Nitric oxide, the enigmatic neuronal messenger: its role in synaptic plasticity. *Trends in Neurosciences* **20**:298–303. doi:10.1016/2236(97)01065-5 ([https://doi.org/10.1016/2236\(97\)01065-5](https://doi.org/10.1016/2236(97)01065-5))
- Imambucus BN, Zhou F, Formozov A, Wittich A, Tenedini FM, Hu C, Sauter K, Macarenhas Varela E, Herédia F, Casimiro AP, Macedo A, Schlegel P, Yang C-H, Miguel-Aliaga I, Wiegert JS, Pankratz MJ, Gontijo AM, Cardona A, Soba P. 2022. A neuropeptidergic circuit gates selective escape behavior of *Drosophila* larvae. *Current Biology* **32**:149–163.e8. doi:10.1016/j.cub.2021.10.069 (<https://doi.org/10.1016/j.cub.2021.10.069>)
- Jacoby J, Nath A, Jessen ZF, Schwartz GW. 2018. A Self-Regulating Gap Junction Network of Amacrine Cells Controls Nitric Oxide Release in the Retina. *Neuron* **100**:1149–1162.e5. doi:10.1016/j.neuron.2018.09.047 (<https://doi.org/10.1016/j.neuron.2018.09.047>)
- Kane EA, Gershoff M, Afonso B, Larderet I, Klein M, Carter AR, Bivort BL de, Sprecher SG, Samuel ADT. 2013. Sensorimotor structure of *Drosophila* larva phototaxis. *Proceedings of the National Academy of Sciences* **110**. doi:10.1073/pnas.1215295110 (<https://doi.org/10.1073/pnas.1215295110>)
- Katoh K, Toh H. 2008. Recent developments in the MAFFT multiple sequence alignment program. *Briefings in Bioinformatics* **9**:286–298. doi:10.1093/bib/bbn013 (<https://doi.org/10.1093/bib/bbn013>)
- Kuehn E, Clausen DS, Null RW, Metzger BM, Willis AD, Özpolat BD. 2021. Segment number threshold determines juvenile onset of germline cluster expansion in *Platynereis dumerilii*. *Journal of Experimental Zoology Part B: Molecular and Developmental Evolution* **338**:225–240. doi:10.1002/jez.b.23100 (<https://doi.org/10.1002/jez.b.23100>)
- Kuntz S, Poeck B, Strauss R. 2017. Visual Working Memory Requires Permissive and Instructive NO/cGMP Signaling at Presynapses in the *Drosophila* Central Brain. *Current Biology* **27**:613–623. doi:10.1016/j.cub.2016.12.056 (<https://doi.org/10.1016/j.cub.2016.12.056>)
- Leise EM, Thavaradhara K, Durham NR, Turner BE. 2001. Serotonin and Nitric Oxide Regulate Metamorphosis in the Marine Snail *Ilyanassa obsoleta*. *American Zoologist* **41**:258–267. doi:10.1093/icb/41.2.258 (<https://doi.org/10.1093/icb/41.2.258>)

- Locascio A, Vassalli QA, Castellano I, Palumbo A. 2022. Novel Insights on Nitric Oxide Synthase and NO Signaling in Ascidian Metamorphosis. *International Journal of Molecular Sciences* **23**:3505. doi:10.3390/ijms23073505 (<https://doi.org/10.3390/ijms23073505>)
- Lundberg JO, Weitzberg E, Shiva S, Gladwin MT. 2011. The nitratenitritenitric oxide pathway in mammals. Humana Press. pp. 21–48. doi:10.1007/978-1-60761-616-0\_3 ([https://doi.org/10.1007/978-1-60761-616-0\\_3](https://doi.org/10.1007/978-1-60761-616-0_3))
- Matsuda S, Harada K, Ito M, Takizawa M, Wongso D, Tsuboi T, Kitaguchi T. 2016. Generation of a cGMP Indicator with an Expanded Dynamic Range by Optimization of Amino Acid Linkers between a Fluorescent Protein and PDE5? *ACS Sensors* **2**:46–51. doi:10.1021/acssensors.6b00582 (<https://doi.org/10.1021/acssensors.6b00582>)
- Mobley RB, Ray EJ, Maruska KP. 2022. Expression and localization of neuronal nitric oxide synthase in the brain and sensory tissues of the African cichlid fish *Astatotilapia burtoni*. *Journal of Comparative Neurology* **530**:2901–2917. doi:10.1002/cne.25383 (<https://doi.org/10.1002/cne.25383>)
- Möller MN, Rios N, Trujillo M, Radi R, Denicola A, Alvarez B. 2019. Detection and quantification of nitric oxide-derived oxidants in biological systems. *Journal of Biological Chemistry* **294**:14776–14802. doi:10.1074/jbc.rev119.006136 (<https://doi.org/10.1074/jbc.rev119.006136>)
- Moroz LL, Meech RW, Sweedler JV, Mackie GO. 2004. Nitric oxide regulates swimming in the jellyfish *Aglantha digitale*. *The Journal of Comparative Neurology* **471**:26–36. doi:10.1002/cne.20023 (<https://doi.org/10.1002/cne.20023>)
- Moroz LL, Romanova DY, Nikitin MA, Sohn D, Kohn AB, Neveu E, Varoqueaux F, Fasshauer D. 2020. The diversification and lineage-specific expansion of nitric oxide signaling in Placozoa: insights in the evolution of gaseous transmission. *Scientific Reports* **10**. doi:10.1038/s41598-020-69851-w (<https://doi.org/10.1038/s41598-020-69851-w>)
- Ozpolat BD, Randel N, Williams EA, Bezares-Calderón LA, Andreatta G, Balavoine G, Bertucci PY, Ferrier DEK, Gambi MC, Gazave E, Handberg-Thorsager M, Hardege J, Hird C, Hsieh Y-W, Hui J, Mutemi KN, Schneider SQ, Simakov O, Vergara HM, Vervoort M, Jékely G, Tessmar-Raible K, Raible F, Arendt D. 2021. The Nereid on the rise: *Platynereis* as a model system. *Zenodo*. doi:10.5281/ZENODO.4907400 (<https://doi.org/10.5281/ZENODO.4907400>)
- Randel N, Asadulina A, Bezares-Calderón LA, Verasztó C, Williams EA, Conzelmann M, Shahidi R, Jékely G. 2014. Neuronal connectome of a sensory-motor circuit for visual navigation. *eLife* **3**. doi:10.7554/elife.02730 (<https://doi.org/10.7554/elife.02730>)
- Santos RM, Lourenço CF, Pomerleau F, Huettl P, Gerhardt GA, Laranjinha J, Barbosa RM. 2011. Brain Nitric Oxide Inactivation Is Governed by the Vasculature. *Antioxidants & Redox Signaling* **14**:1011–1021. doi:10.1089/ars.2010.3297 (<https://doi.org/10.1089/ars.2010.3297>)
- Shettigar N, Chakravarthy A, Umashankar S, Lakshmanan V, Palakodeti D, Gulyani A. 2021. Discovery of a body-wide photosensory array that matures in an adult-like animal and mediates eyebrain-independent movement and arousal. *Proceedings of the National Academy of Sciences* **118**. doi:10.1073/pnas.2021426118 (<https://doi.org/10.1073/pnas.2021426118>)
- Shu CJ, Ulrich LE, Zhulin IB. 2003. The NIT domain: a predicted nitrate-responsive module in bacterial sensory receptors. *Trends in Biochemical Sciences* **28**:121–124. doi:10.1016/s0968-0004(03)00032-x ([https://doi.org/10.1016/s0968-0004\(03\)00032-x](https://doi.org/10.1016/s0968-0004(03)00032-x))
- Song H, Hewitt OH, Degnan SM. 2021. Arginine Biosynthesis by a Bacterial Symbiont Enables Nitric Oxide Production and Facilitates Larval Settlement in the Marine-Sponge Host. *Current Biology* **31**:433–437.e3. doi:10.1016/j.cub.2020.10.051 (<https://doi.org/10.1016/j.cub.2020.10.051>)
- Tessmar-Raible K, Steinmetz PRH, Snyman H, Hassel M, Arendt D. 2005. Fluorescent two-color whole mount *in situ* hybridization in *Platynereis dumerilii* (Polychaeta, Annelida), an emerging marine molecular model for evolution and development. *BioTechniques* **39**:460–464. doi:10.2144/000112023 (<https://doi.org/10.2144/000112023>)
- Thomas DD. 2015. Breathing new life into nitric oxide signaling: A brief overview of the interplay between oxygen and nitric oxide. *Redox Biology* **5**:225–233. doi:10.1016/j.redox.2015.05.002 (<https://doi.org/10.1016/j.redox.2015.05.002>)
- Tooker RE, Lipin MY, Leuranguer V, Rozsa E, Bramley JR, Harding JL, Reynolds MM, Vigh J. 2013. Nitric Oxide Mediates Activity-Dependent Plasticity of Retinal Bipolar Cell Output via S-Nitrosylation. *The Journal of Neuroscience* **33**:19176–19193. doi:10.1523/jneurosci.2792-13.2013 (<https://doi.org/10.1523/jneurosci.2792-13.2013>)
- Tosches MA, Bucher D, Vopalensky P, Arendt D. 2014. Melatonin Signaling Controls Circadian Swimming Behavior in Marine Zooplankton. *Cell* **159**:46–57. doi:10.1016/j.cell.2014.07.042 (<https://doi.org/10.1016/j.cell.2014.07.042>)
- Tsukamoto H, Chen I-S, Kubo Y, Furutani Y. 2017. A ciliary opsin in the brain of a marine annelid zooplankton is ultraviolet-sensitive, and the sensitivity is tuned by a single amino acid residue. *Journal of Biological Chemistry* **292**:12971–12980. doi:10.1074/jbc.m117.793539 (<https://doi.org/10.1074/jbc.m117.793539>)

- Tsukamoto H, Kubo Y. 2023. A self-inactivating invertebrate opsin optically drives biased signaling toward G $\beta\gamma$ -dependent ion channel modulation. *Proceedings of the National Academy of Sciences* **120**. doi:10.1073/pnas.2301269120 (<https://doi.org/10.1073/pnas.2301269120>)
- Ueda N, Richards GS, Degnan BM, Kranz A, Adamska M, Croll RP, Degnan SM. 2016. An ancient role for nitric oxide in regulating the animal pelagobenthic life cycle: evidence from a marine sponge. *Scientific Reports* **6**. doi:10.1038/srep37546 (<https://doi.org/10.1038/srep37546>)
- Veedin Rajan VB, Häfker NS, Arboleda E, Poehn B, Gossenreiter T, Gerrard E, Hofbauer M, Mühlstein C, Bileck A, Gerner C, Ribera d'Alcalá M, Buia MC, Hartl M, Lucas RJ, Tessmar-Raible K. 2021. Seasonal variation in UVA light drives hormonal and behavioural changes in a marine annelid via a ciliary opsin. *Nature Ecology & Evolution* **5**:204–218. doi:10.1038/s41559-020-01356-1 (<https://doi.org/10.1038/s41559-020-01356-1>)
- Verasztó C, Gühmann M, Jia H, Rajan VB, Bezires-Calderón LA, Piñeiro-Lopez C, Randel N, Shahidi R, Michiels NK, Yokoyama S, Tessmar-Raible K, Jékely G. 2018. Ciliary and rhabdomeric photoreceptor-cell circuits form a spectral depth gauge in marine zooplankton. *eLife* **7**. doi:10.7554/elife.36440 (<https://doi.org/10.7554/elife.36440>)
- Verasztó C, Jasek S, Gühmann M, Shahidi R, Ueda N, Beard JD, Mendes S, Heinz K, Bezires-Calderón LA, Williams E, Jékely G. 2020. Whole-animal connectome and cell-type complement of the three-segmented *Platynereis dumerilii* larva (<http://dx.doi.org/10.1101/2020.08.21.260984>).
- Verasztó C, Ueda N, Bezires-Calderón LA, Panzera A, Williams EA, Shahidi R, Jékely G. 2017. Ciliomotor circuitry underlying whole-body coordination of ciliary activity in the *Platynereis* larva. *eLife* **6**. doi:10.7554/elife.26000 (<https://doi.org/10.7554/elife.26000>)
- Vergara HM, Pape C, Meechan KI, Zinchenko V, Genoud C, Wanner AA, Mutemi KN, Titze B, Templin RM, Bertucci PY, Simakov O, Dürichen W, Machado P, Savage EL, Schermelleh L, Schwab Y, Friedrich RW, Kreshuk A, Tischer C, Arendt D. 2021. Whole-body integration of gene expression and single-cell morphology. *Cell* **184**:4819–4837.e22. doi:10.1016/j.cell.2021.07.017 (<https://doi.org/10.1016/j.cell.2021.07.017>)
- Vielma AH, Agurto A, Valdés J, Palacios AG, Schmachtenberg O. 2014. Nitric Oxide Modulates the Temporal Properties of the Glutamate Response in Type 4 OFF Bipolar Cells. *PLoS ONE* **9**:e114330. doi:10.1371/journal.pone.0114330 (<https://doi.org/10.1371/journal.pone.0114330>)
- Wang G-Y, List DA van der, Nemargut JP, Coombs JL, Chalupa LM. 2007. The sensitivity of light-evoked responses of retinal ganglion cells is decreased in nitric oxide synthase gene knockout mice. *Journal of Vision* **7**:7. doi:10.1167/7.14.7 (<https://doi.org/10.1167/7.14.7>)
- Wei T, Schubert T, Paquet-Durand F, Tanimoto N, Chang L, Koeppen K, Ott T, Griesbeck O, Seeliger MW, Euler T, Wissinger B. 2012. Light-Driven Calcium Signals in Mouse Cone Photoreceptors. *Journal of Neuroscience* **32**:6981–6994. doi:10.1523/jneurosci.6432-11.2012 (<https://doi.org/10.1523/jneurosci.6432-11.2012>)
- Wildemann B, Bicker G. 1999. Developmental expression of nitric oxide/cyclic GMP synthesizing cells in the nervous system of *Drosophila melanogaster*. *Journal of Neurobiology* **38**:1–15. doi:10.1002/(sici)1097-4695(199901)38:1<1::aid-neu1>3.0.co;2-l ([https://doi.org/10.1002/\(sici\)1097-4695\(199901\)38:1<1::aid-neu1>3.0.co;2-l](https://doi.org/10.1002/(sici)1097-4695(199901)38:1<1::aid-neu1>3.0.co;2-l))
- Williams EA, Verasztó C, Jasek S, Conzelmann M, Shahidi R, Bauknecht P, Mirabeau O, Jékely G. 2017. Synaptic and peptidergic connectome of a neurosecretory center in the annelid brain. *eLife* **6**. doi:10.7554/elife.26349 (<https://doi.org/10.7554/elife.26349>)
- Zhang Y, He L-S, Zhang G, Xu Y, Lee O-O, Matsumura K, Qian P-Y. 2012. The regulatory role of the NO/cGMP signal transduction cascade during larval attachment and metamorphosis of the barnacle *Balanus* (= *Amphibalanus amphitrite*). *Journal of Experimental Biology*. doi:10.1242/jeb.070235 (<https://doi.org/10.1242/jeb.070235>)

## Figure supplements



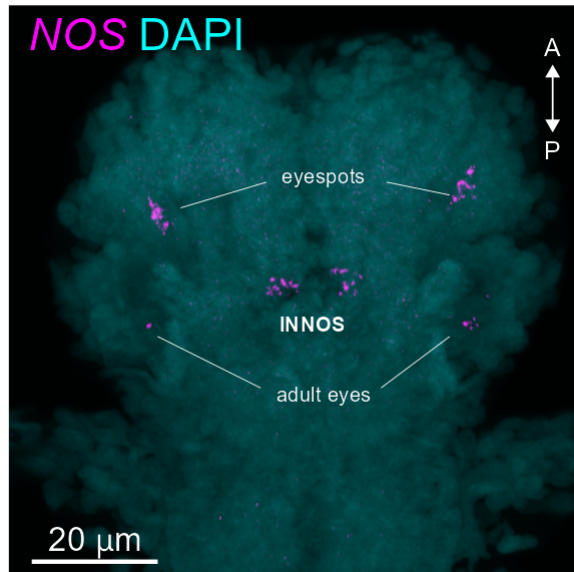
**Figure 1 – figure supplement 1. Maximum-likelihood phylogenetic tree of NOS protein sequences.** Individual branches are coloured by taxonomy. Branch support values indicate UFBoot and aLRT-SH-like values.

Figure 1 – figure supplement 1 – source data 1. NOS sequences used for the phylogenetic reconstruction.

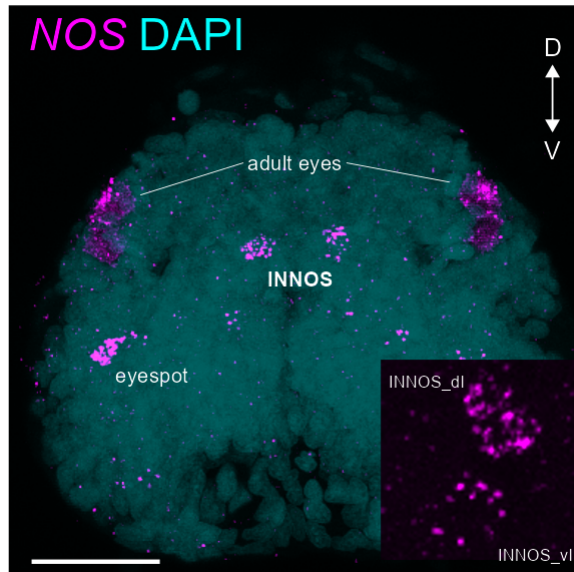
Figure 1 – figure supplement 1 – source data 2. Aligned and trimmed NOS sequences used for the phylogenetic reconstruction.

Figure 1 – figure supplement 1 – source data 3. Tree file of the reconstructed NOS phylogeny.

## A in situ HCR



## B in situ HCR



**Figure 1 – figure supplement 2. Expression of NOS in three-day-old *Platynereis* larva.** **(A)** HCR in situ for NOS (magenta), dorsal view. **(B)** HCR in situ for NOS (magenta), ventral view. Inset in **(B)** shows close-up of two NOS-positive cells (INNOS\_dl and INNOS\_vl) on the left side. Samples were also stained for DAPI (cyan) to label nuclei.

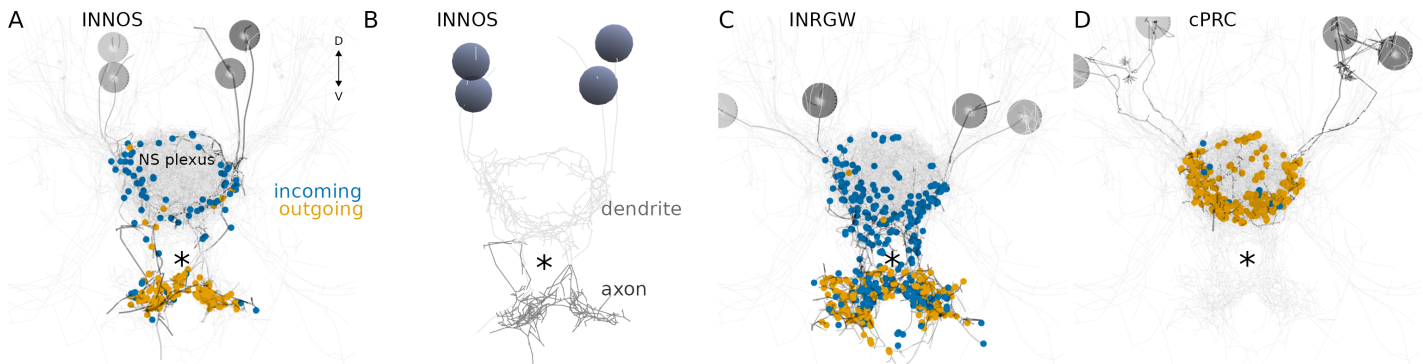


**Figure 1 – figure supplement 3. Synapse distribution in cPRCs and possynaptic interneurons** **(A)** Volume rendering of the four INNOS neurons with incoming and outgoing synapses. **(B)** Axo-dendritic splitting of the INNOS neurons. **(C)** Volume rendering of the four INRGW neurons with incoming and outgoing synapses. **(D)** Volume rendering of the four cPRC neurons with incoming and outgoing synapses. All images are anterior views. Asterisk marks the same position across images for reference. Grey speheres indicate the position of cell nuclei. NS plexus; neurosecretory plexus. The radius of INNOS nuclei is set to 2  $\mu$ m for scale.

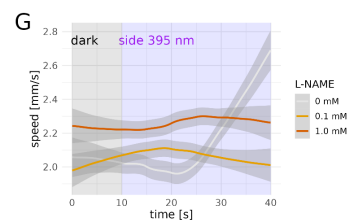
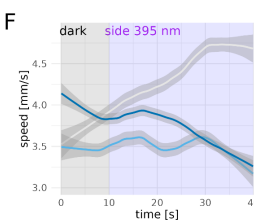
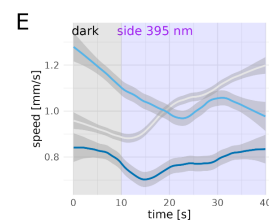
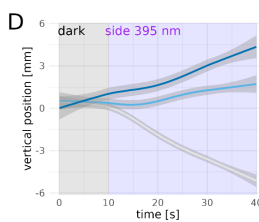
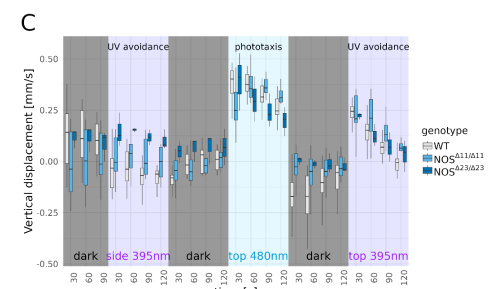
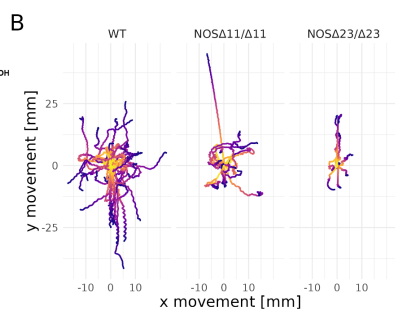
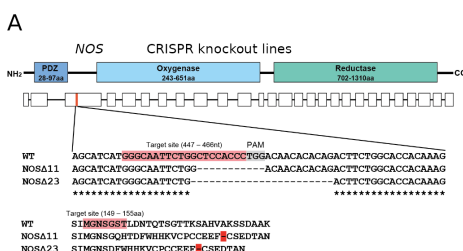


**Figure 3 – figure supplement 1. Generation and behavioural characterisation of NOS CRISPR knockouts.** **(A)** Top: The domain organisation of *Platynereis* NOS protein and exon/intron structure of the NOS gene. Bottom: The genomic locus of

NOS with the CRISPR target site, wild-type and knockout ( $\text{NOS}\Delta 11$ ,  $\text{NOS}\Delta 23$ ) sequences and predicted protein sequences. The PAM sequence is shown in grey, stop codons in red. **(B)** Swimming trajectories of wild type (WT, n=37) and NOS mutant ( $\text{NOS}\Delta 11/\Delta 11$ , n=18 and  $\text{NOS}\Delta 23/\Delta 23$ , n=8) two-day-old larvae. All trajectories start at 0 x and y position and time 0 corresponding to 10 sec after the onset of 395 nm stimulation from the side. **(C)** Vertical displacement in 30 sec bins of wild type and mutant ( $\text{NOS}\Delta 11$  and  $\text{NOS}\Delta 23$ ) two-day-old larvae stimulated with 395 nm light from the side, 488 nm light from the top and 395 nm light from the top. **(D)** Vertical position of batches of wild type and mutant two-day-old larvae over time under 395 nm UV stimulation. The starting position of each larval trajectory was set to 0. **(E-G)** Swimming speed of batches of wild type and mutant two-day old (E) and three-day-old (F) larvae and L-NAME-treated (NOS inhibitor) three-day-old larvae under 395 nm UV stimulation.

Figure 3 – figure suppmenet 1 – source data 1-6. Source data for panels B-G.

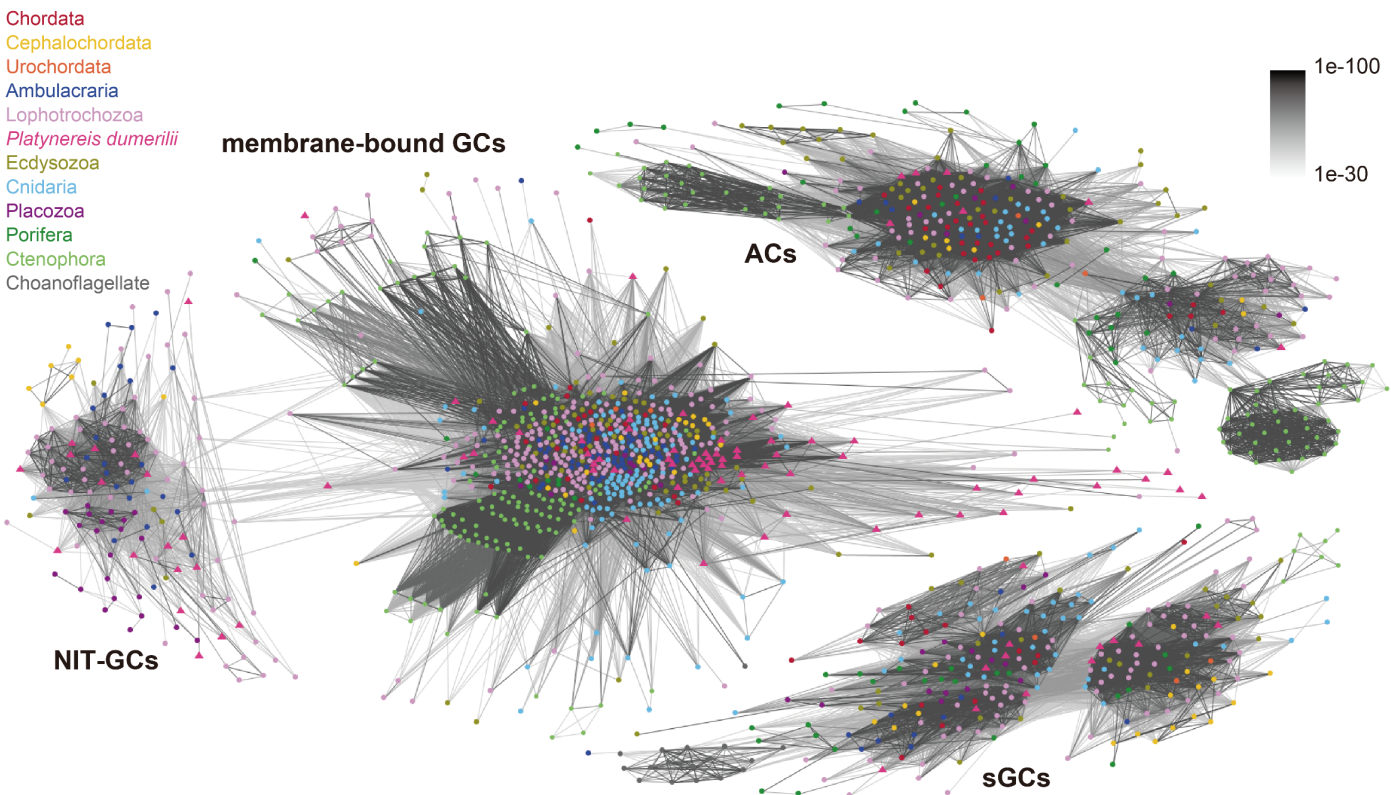


**Figure 4 – figure supplement 1. Cluster analysis of guanylate and adenylate cyclase sequences.** Each node represents one sequence, colour-coded by taxonomy. Connections represent BLAST P-values of <1e-16. NIT-GCs, NIT domain containing guanylate cyclases; membrane-bound GCs, membrane-bound guanylate cyclases; sGCs, soluble guanylate cyclases; ACs, adenylate cyclases.

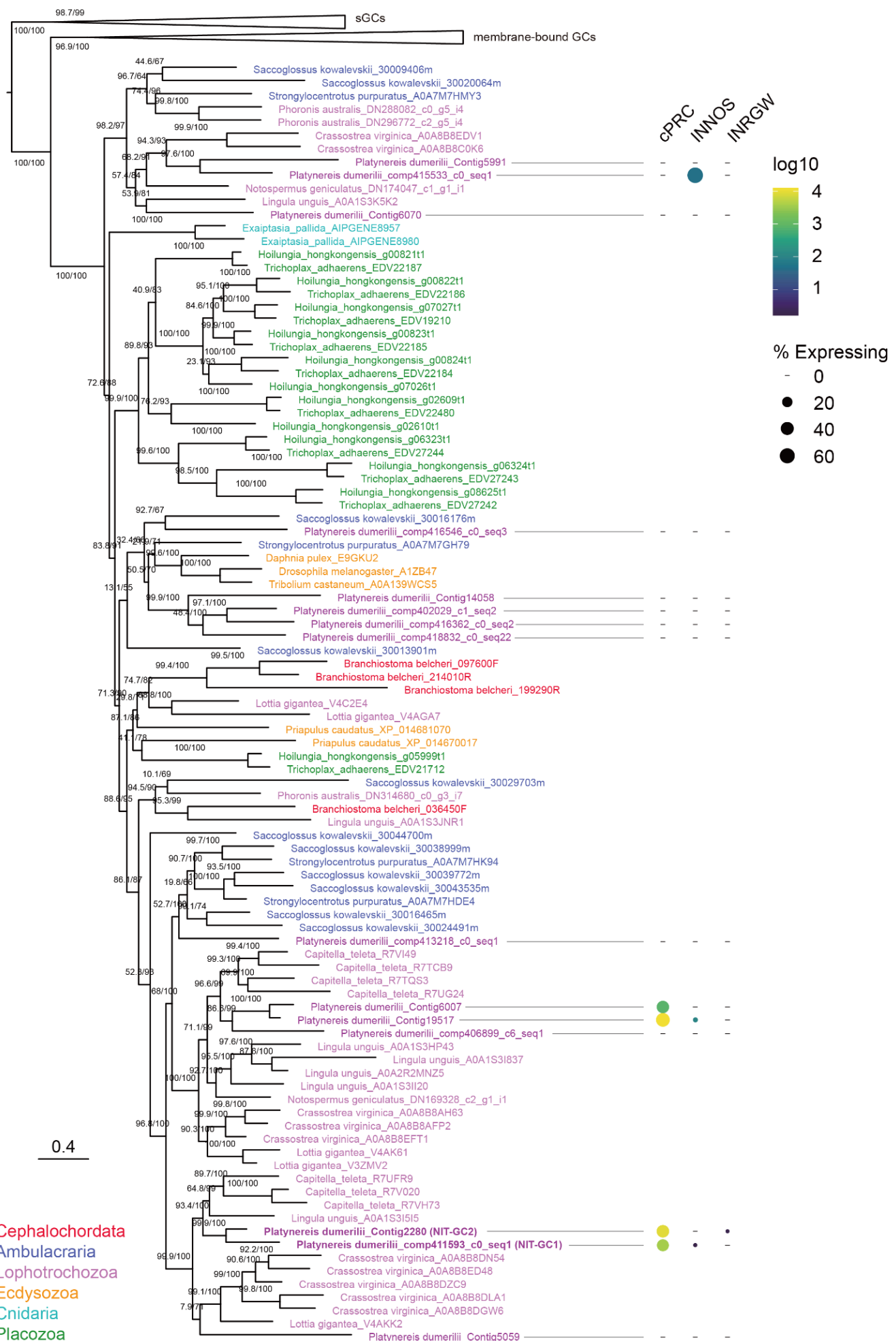


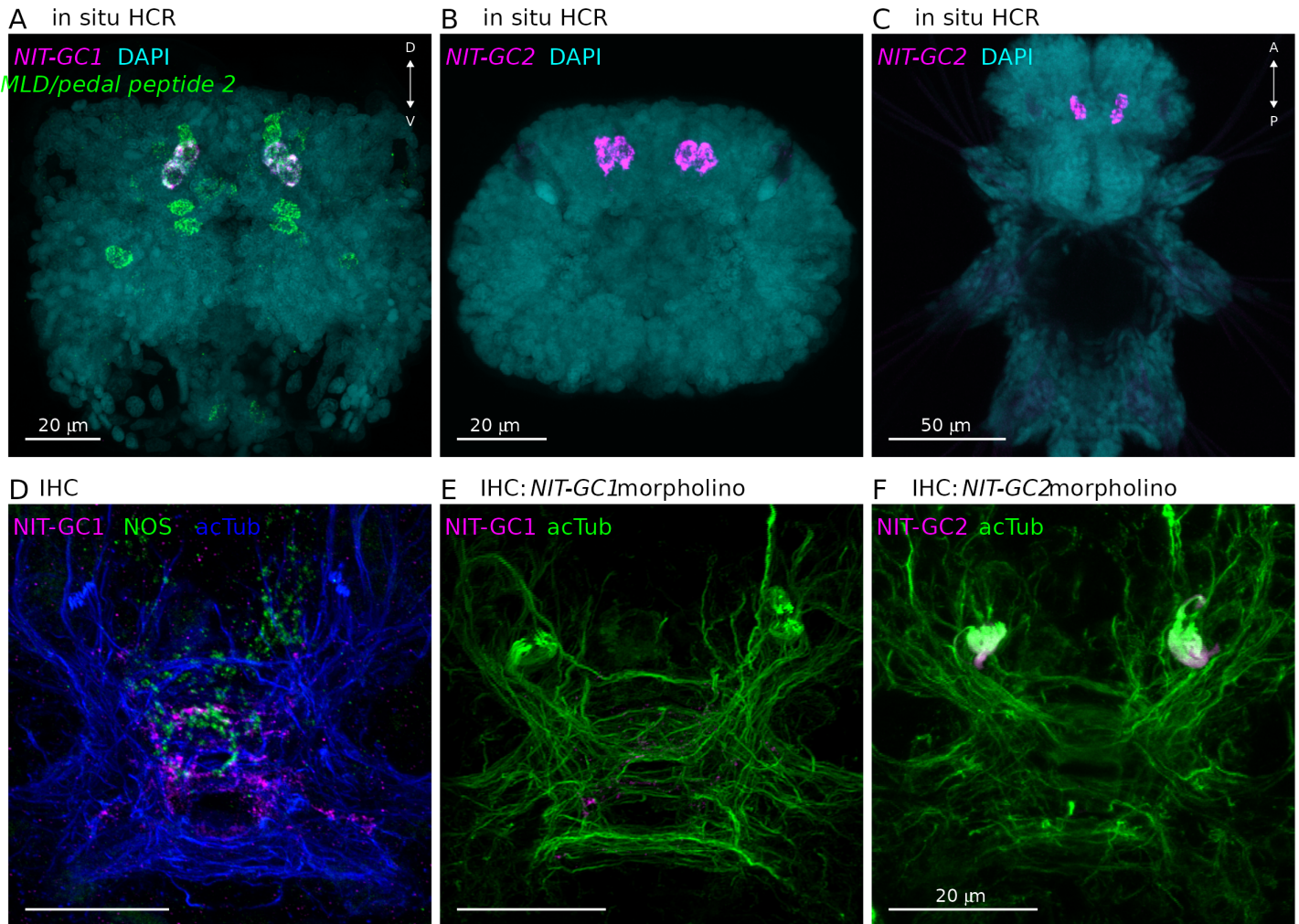
**Figure 4 – figure supplement 2. Maximum-likelihood phylogenetic tree of NIT-domain-containing guanylate cyclases**  
Membrane-bound and soluble guanylate cyclases (sGC) were included as outgroups. Guanylate cyclases with NIT domains

are found in most animal phyla except Porifera, Ctenophora, Urochordata and Chordata. Branch support values indicate UFBoot and aLRT-SH-like values. The expression of *Platynereis* NIT-GC genes in cPRC, INNOS and INRGW cells is indicated on the right side of the tree. The values represent expression based on single-cell sequencing data. Dot size indicates specificity (percent of transcripts expressed in the indicated cell across all cells). Dot colour represents the logarithm of the number of transcripts in the expressing cells.

Figure 4 – figure supplement 2 – source data 1. GC sequences used for the phylogenetic reconstruction.

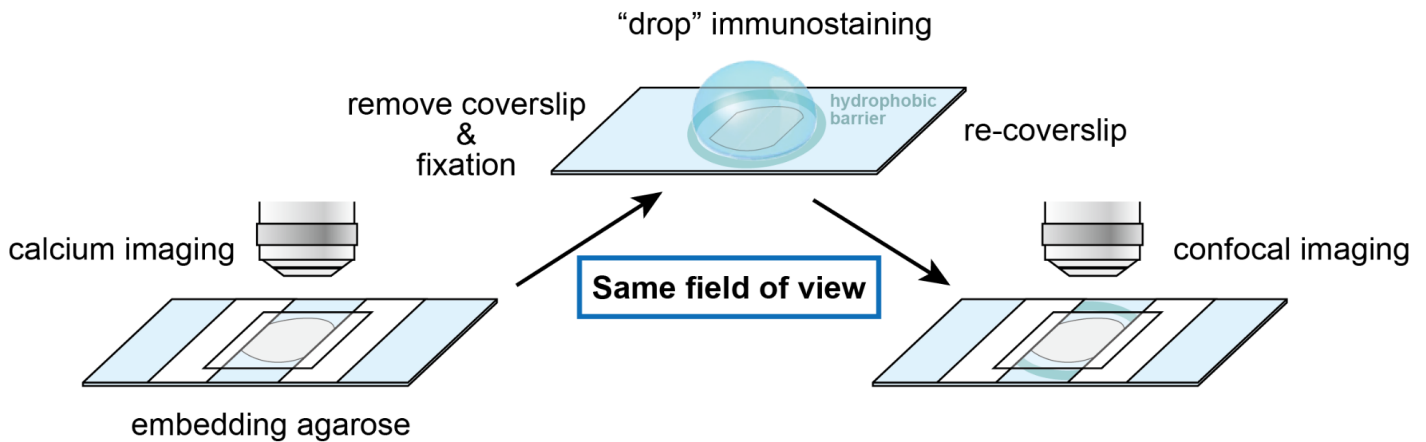
Figure 4 – figure supplement 2 – source data 2. Aligned and trimmed GC sequences used for the phylogenetic reconstruction.

Figure 4 – figure supplement 3 – source data 3. Tree file of the reconstructed GC phylogeny.

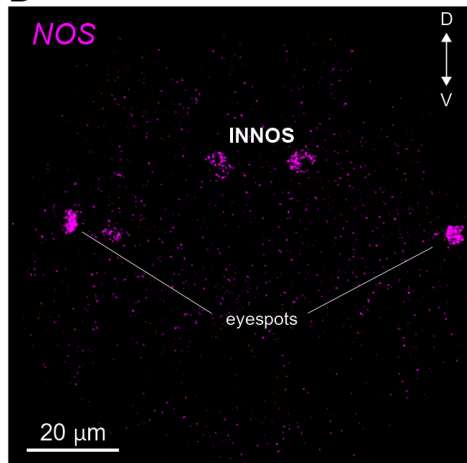


**Figure 4 – figure supplement 3. Expression of NIT-GC1 and NIT-GC2 in the cPRCs** **(A)** HCR co-expression analysis of *NIT-GC1* (magenta) and *MLD/pedal-peptide-2* proneuropeptide (green). Anterior view of a two-day-old larva. Nuclei were stained with DAPI (cyan). **(B, C)** Expression of *NIT-GC2* (magenta) detected by in situ HCR. Anterior (B) and ventral (C) views of a three-day-old larva. Nuclei were stained with DAPI (cyan). **(D)** Immunostaining for *NIT-GC1* (magenta) and *NOS* (green). Anterior view of a two-day-old larva. Acetylated α-tubulin staining (blue) highlights the neuropil and cPRC cilia. **(E, F)** Immunostaining for *NIT-GC1* (E) and *NIT-GC2* (F) antibodies in larvae injected with *NIT-GC1* (E) or *NIT-GC2* (F) morpholinos. Acetylated α-tubulin staining (green) highlights the neuropil and cPRC cilia. Anterior view of a two-day-old larva.

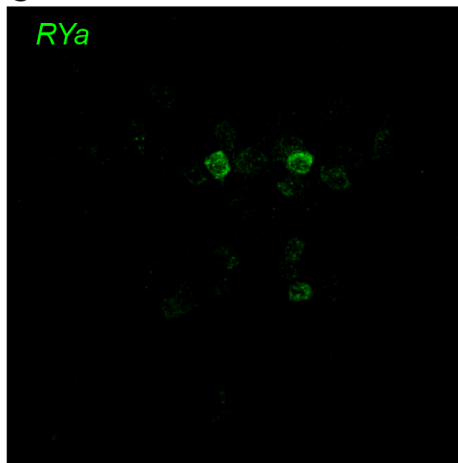
A



B in situ HCR



C



D

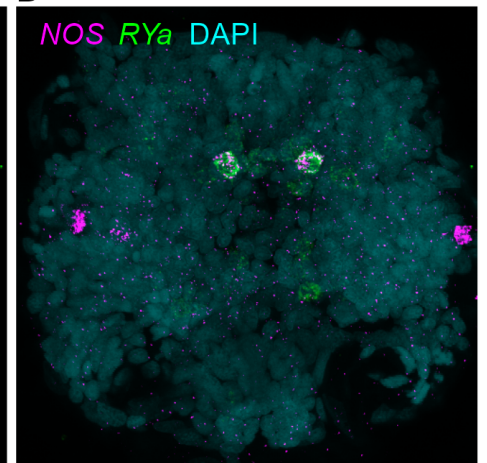


**Figure 5 – figure supplement 1. On-slide immunostaining and coexpression analysis of NOS and RYamide proneuropeptide (A) Schematic diagram of the on-slide immunostaining procedure after  $\text{Ca}^{2+}$  imaging.(B-D) Co-expression analysis by HCR in situ of NOS (magenta) and RYamide proneuropeptide (green). Anterior view of a two-day-old larva. Nuclei were stained by DAPI (cyan).**

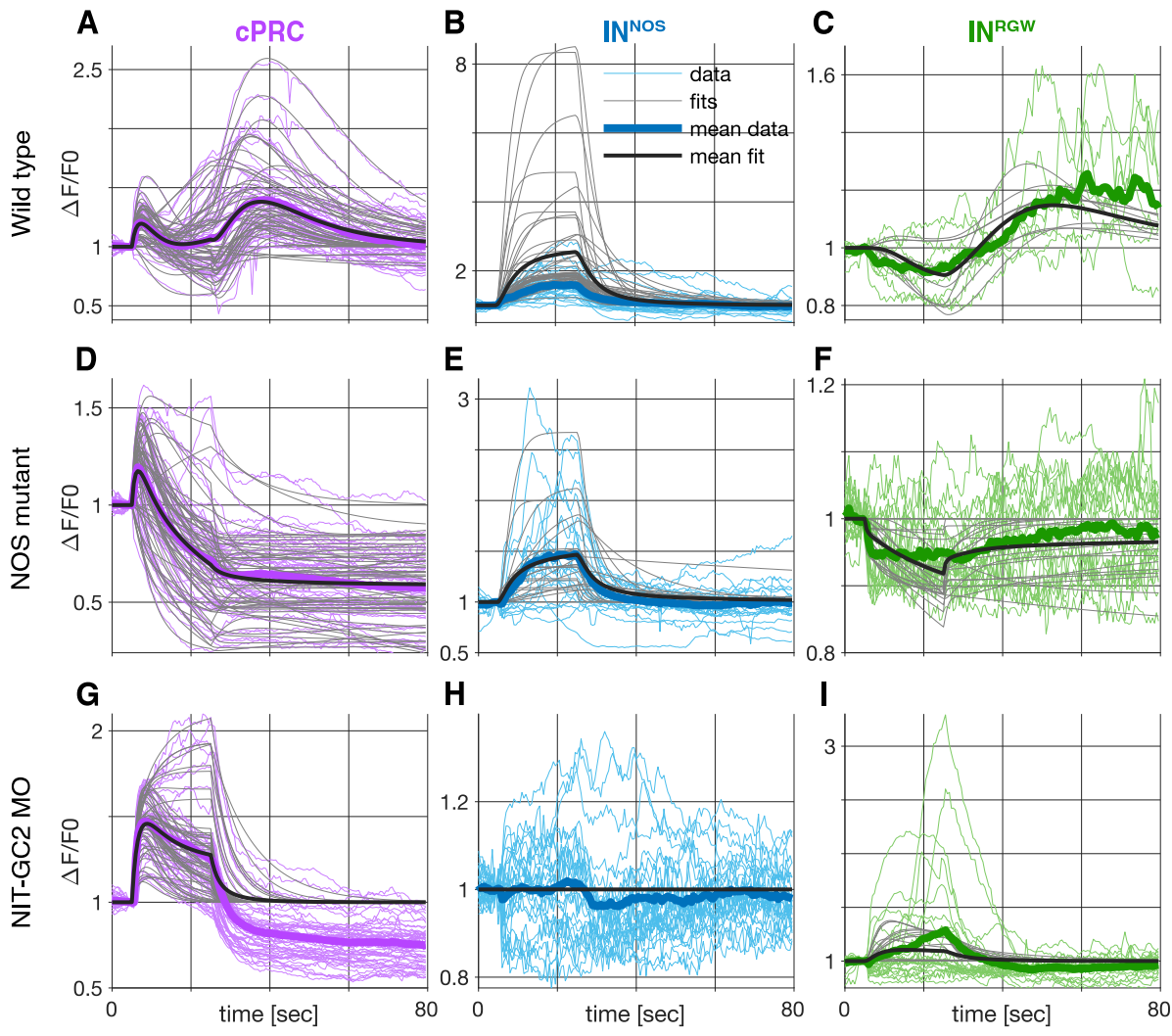


**Figure 6 – figure supplement 1. Simulated  $\text{Ca}^{2+}$  traces for parameter sets fitted to individual  $\text{Ca}^{2+}$ -recordings collected in wild type, NOS knockout, and *NIT-GC2* morphant larvae.** (A-C) Simulated  $\text{Ca}^{2+}$  traces in cPRC (A), INNOS (B) and INRGW (C) cells in the wild-type condition. (D-F) Simulated  $\text{Ca}^{2+}$  traces in cPRC (D), INNOS (E) and INRGW (F) cells in the NOS-knockout condition. (G-I) Simulated  $\text{Ca}^{2+}$  traces in cPRC (G), INNOS (H) and INRGW (I) cells in the *NIT-GC2*-morphant condition. Thin coloured curves indicate individual recordings (cPRC - purple, INNOS - blue and INRGW - green), thin grey curves indicate simulated  $\text{Ca}^{2+}$  traces based on model parameters fitted to the individual recording, thick coloured curves indicate averages of the recordings and thick black curves represent the average of the fits.

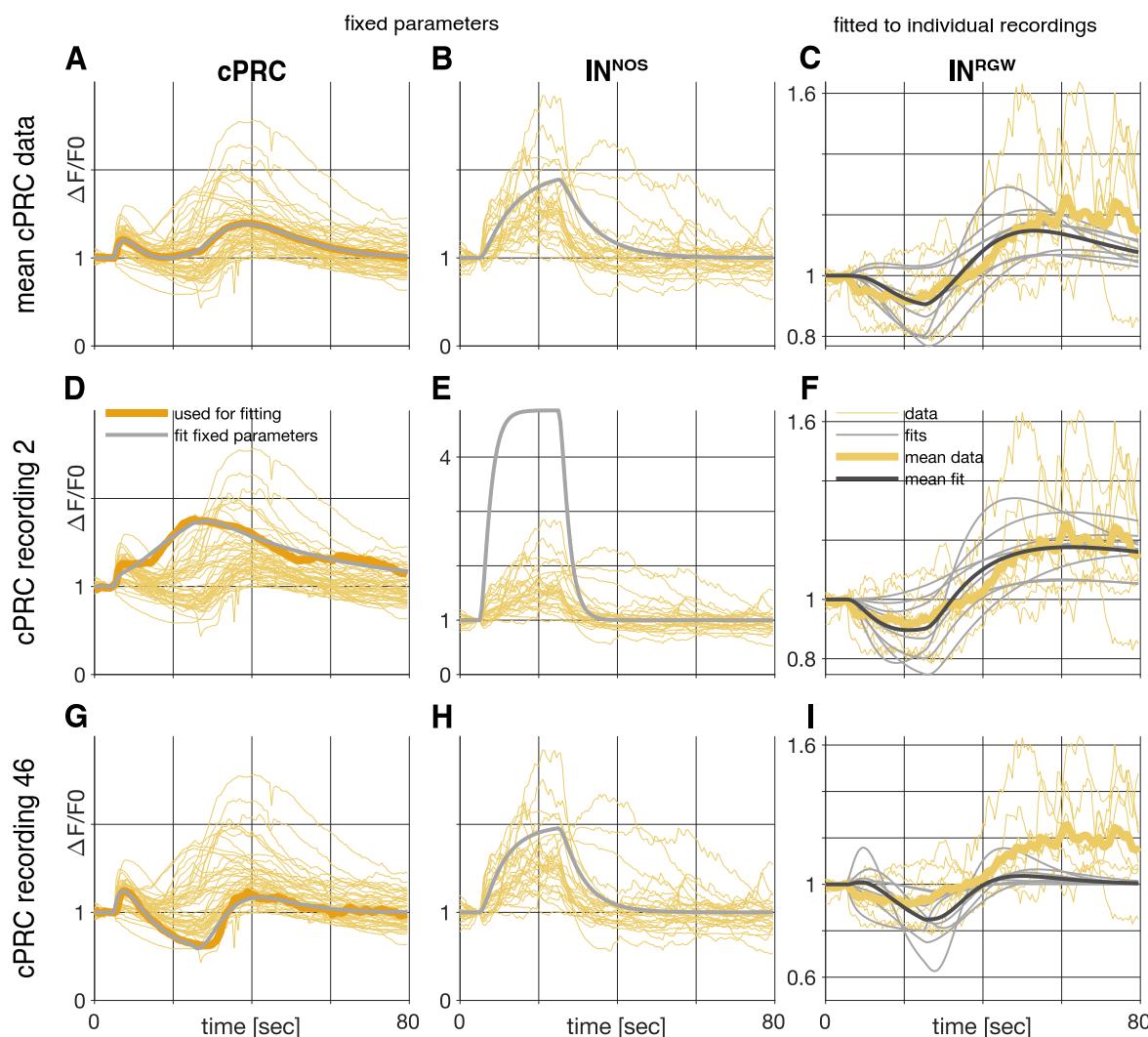


**Figure 6 – figure supplement 2. Comparison of fits with different fixed parameter sets when fitting the WT model to individual recordings from the WT INRGW cells.** Panels A-B, D-E, G-H (column fixed parameters) show simulated traces of the  $\text{Ca}^{2+}$  levels in cPRC and INNOS cells produced by different fixed parameter sets. Panels C, F and I show individual recordings fitted to the data from INRGW cells.

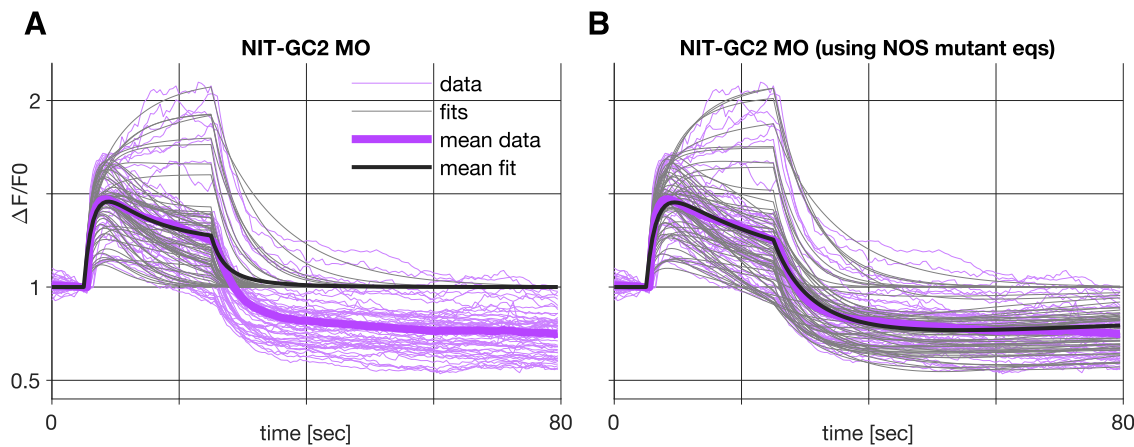


**Figure 6 – figure supplement 3. Comparison of fits to the cPRC recordings from NIT-GC2 morphant larvae using the NIT-GC2 morpholino model or the NOS-knockout model.** Thin coloured curves indicate individual recordings, thin grey curves are simulated  $\text{Ca}^{2+}$  traces, thick coloured curves indicate averages of the recordings and thick black curves represent the mean of the fits.

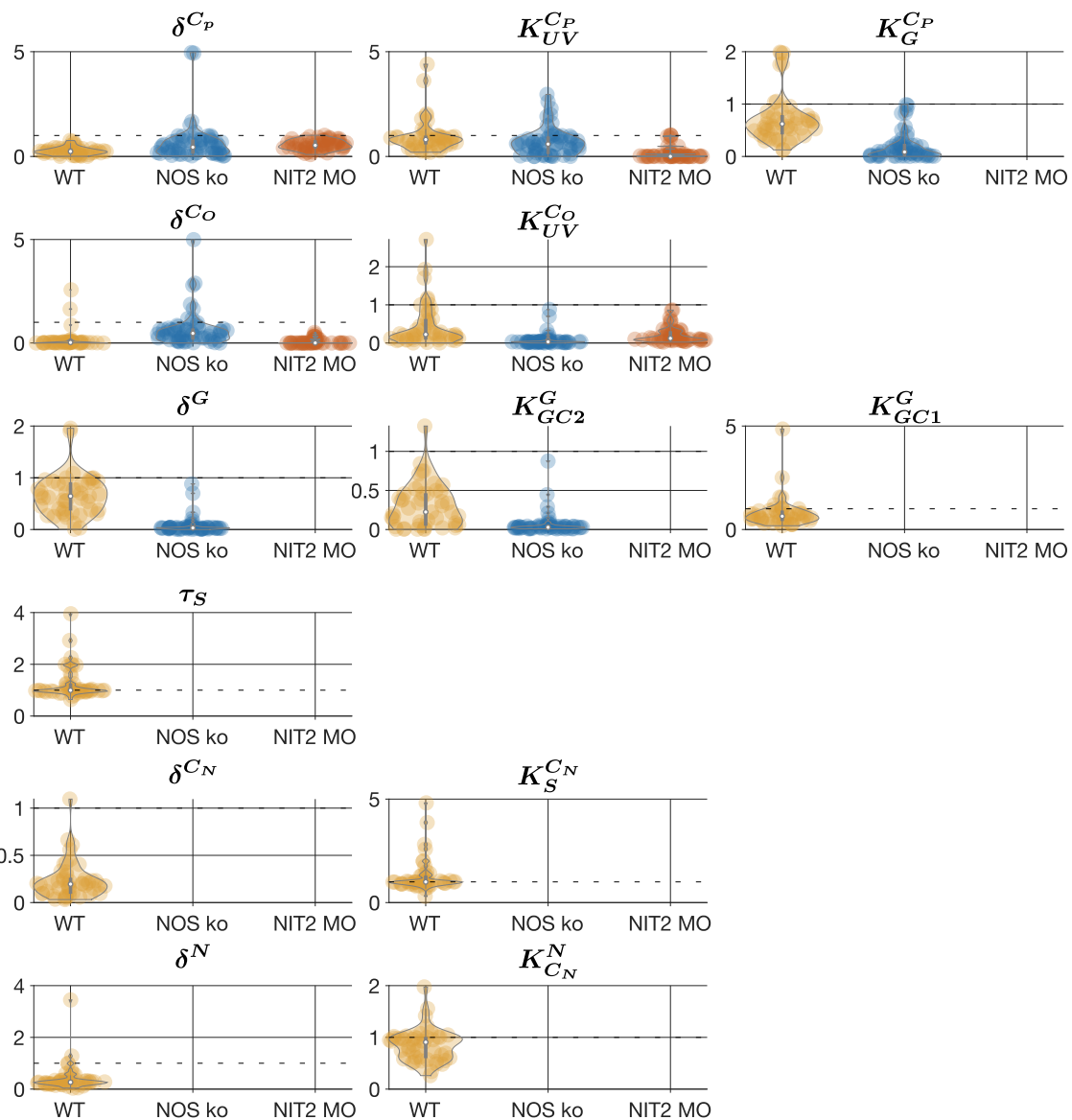


**Figure 6 – figure supplement 4. Distributions of the parameter values fitted to the cPRC recordings.** Violin plots (grey lines) are kernel density estimates of the underlying distributions; computed using the Matlab function *ksdensity* with default settings, i.e., using normal kernel function, plots are trimmed to the observed range of data. Markers represent individual parameter values, white markers indicate medians, vertical grey bars indicate interquartile range (Q25 to Q75), and the dashed line indicates the value 1. Where violin plots are not shown, these parameters are associated with terms/equations that are excluded from the fitting procedure (see Methods for details).

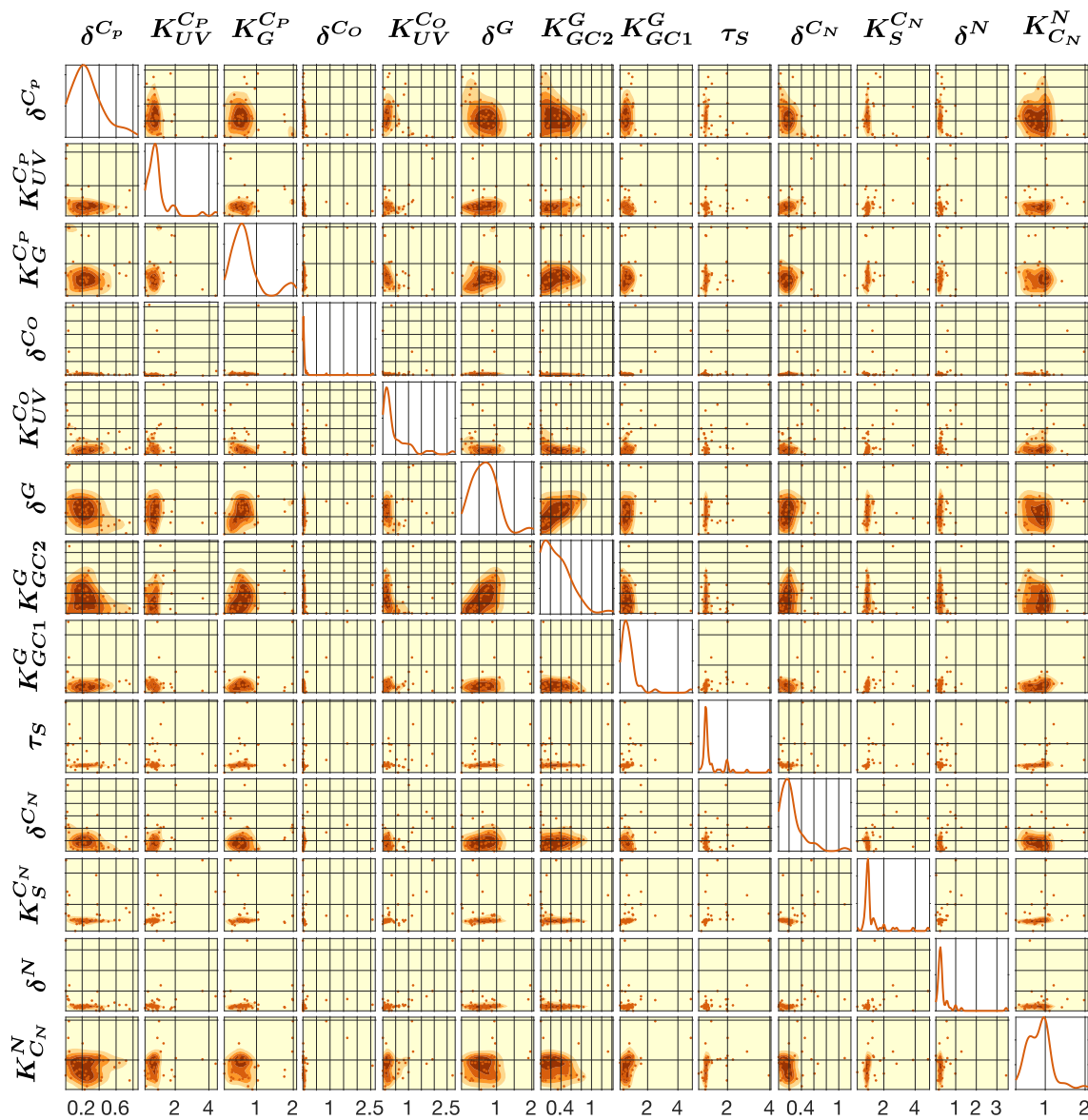


**Figure 6 – figure supplement 5. Pairwise correlations between parameters of the WT model fitted to WT cPRC recordings**

Parameters associated with the  $C_R$  equation are not included (see Methods for details). Panels on the diagonal show kernel density estimates of the distributions of the individual parameters; computed using Matlab function *ksdensity* with default settings, i.e., using normal kernel function, plots are trimmed to the observed range of data. The other panels show kernel density estimates of bivariate distributions of pairs of parameters (heatmaps; darker colours indicate higher density). Also shown using markers are the values of the individual parameter combinations.